Fuel 255 (2019) 115642

Contents lists available at ScienceDirect

Fuel

journal homepage: www.elsevier.com/locate/fuel

Full Length Article

Experimental investigation of pilot-fuel combustion in dual-fuel engines, Part 1: Thermodynamic analysis of combustion phenomena

Aleš Srna[a,*], Beat von Rotz[a], Kai Herrmann[b], Konstantinos Boulouchos[c], Gilles Bruneaux[d]

[a] Paul Scherrer Institute, Energy and Environment Division, Forschungstrasse 111, CH-5232 Villigen PSI, Switzerland
[b] University of Applied Sciences and Arts Northwestern Switzerland, Institute of Thermal and Fluid Engineering, School of Engineering, Klosterzelgstrasse 2, CH-5210 Windisch, Switzerland
[c] ETH Zürich, Institute for Energy Technology, Laboratory for Aerothermochemistry and Combustion Systems, Sonneggstrasse 3, CH-8092 Zürich, Switzerland
[d] Institut Carnot IFPEN Transports Energie, IFP Energies Nouvelles, 1 et 4 Avenue de Bois Préau, 92852 Rueil-Malmaison, France

ARTICLE INFO

Keywords:
Dual-fuel engines
Natural-gas engines
Combustion mode transition
Autoignition
Tracer-PLIF
Combustion phenomenology

ABSTRACT

The pilot-fuel auto-ignition and combustion in compressed methane/air mixtures are investigated. Experiments were performed in an optically accessible rapid compression-expansion machine featuring quiescent charge conditions and a single-hole coaxial diesel injector mounted on the cylinder periphery. It enabled thermodynamic analysis of the pilot-fuel combustion without these phenomena being masked by the rapid premixed-flame propagation like in the engine test rigs with turbulent charge. The aim of this study is to elucidate the first-order influences of charge and pilot-fuel parameters on the ignition delay and transition into the premixed flame propagation. For this purpose, a comprehensive measurement matrix including variations of the premixed fuel equivalence ratio, charge temperature, and oxygen content as well as the variation of pilot injection duration is tested. The heat release rate (HRR) metrics describing the pilot-fuel combustion duration, peak HRR, and cumulative HRR during the pilot-fuel combustion are derived. Correlations of the HRR metrics to the ignition delay, pilot-fuel mixing state at ignition and the volume of the pilot-fuel jet are investigated. Methane is found to increase the ignition delay and prolong the pilot-fuel combustion duration. This effect is amplified for pilot-injection strategies with leaner pilot-fuel mixtures at ignition or in the case of reduced charge oxygen content. Despite the reduced pilot-fuel reactivity the co-combustion of entrained methane leads to higher peak-HRR, except in the reduced charge oxygen cases, where the excessively reduced mixture reactivity with the introduction of methane leads even to a reduced peak-HRR.

The phenomenology of the dual-fuel combustion process is described in Part 1, whereas Part 2 of this work aims at improving the understanding of the underlying processes by application of advanced optical diagnostic methods.

1. Introduction

In the recent years, many gas-fueled engine concepts emerged, for transportation as well as stationary applications. They are seen to be an attractive solution to meet the current and upcoming emission legislation. The application of natural gas is advantageous regarding the associated CO_2 reduction, high resistance to auto-ignition (knock) and low sooting propensity. Especially in the large engine applications ranging from heavy-duty to marine and stationary, the lean burn combustion systems with a potential for lower pollutant emission at diesel-engine comparable efficiencies [1] are employed. Nevertheless, efficiency and combustion stability often deteriorate at low loads. Therefore, the advanced ignition systems like pilot-injection or pre-chamber spark-ignition are utilized to ensure stable and fast

Abbreviations: [O_2], Charge oxygen concentration [vol %]; aSOI, after Start of Injection; BDC, Bottom Dead Center; EGR, Exhaust Gas Recirculation; EOI, End of Injection; eSOI, Electronic start of injection; ET, injector Energizing Time; FHWM, Full-Width at Half-Maximum; HRR, Heat Release Rate; HRR_{pilot}^{MAX}, Pilot-combustion peak HRR; ID, Ignition Delay; LHV, Lower Heating Value; m_v, Wiebe-function shape parameter; NO_x, Nitrogen oxides; p_{inj}, Injection pressure; PIV, Particle Image Velocimetry; PLIF, Planar Laser-Induced Fluorescence; RCCI, Reactivity-Controlled Compression Ignition; RCEM, Rapid Compression-Expansion Machine; SOI, hydraulic Start of Injection; TDC, Top Dead Center; TMPD, N,N,N',N' – tetramethyl-p-phenilenediamine; T_{SOI}, Charge temperature at SOI; t_v, Pilot-fuel combustion duration metric; UHC, Unburnt HydroCarbons; ϕ_{CH4}, Charge methane equivalence ratio

* Corresponding author.
E-mail address: ales.srna@alumni.ethz.ch (A. Srna).

https://doi.org/10.1016/j.fuel.2019.115642
Received 19 November 2018; Received in revised form 28 March 2019; Accepted 11 June 2019
Available online 29 June 2019

combustion. In combination with further measures such as exhaust gas recirculation and variable valve timing to additionally increase the cycle efficiency, this technology is promising as a solution in short to midterm perspective to fulfill the stricter emission legislation.

Studies in full engines [2–5], single cylinder engines [6–12], optical engines [13–17] and more generic devices such as rapid compression machines [18–22] are documented. Most of the engine related studies were focusing on the analysis of the heat release rate stability and characteristics as well as the exhaust gas emissions. A common approach is substituting part of the diesel fuel (reduction of injection duration) with premixed methane showing a potential for significant NO_x and soot reduction. Nevertheless, especially under the low loads, the combustion duration is considerably prolonged resulting in a worse thermal efficiency [2–4,6–9]. The adverse effect seen in dual-fuel engines (gas mode operation) is obviously the increase in UHC emission which shows up to two orders of magnitude higher emission levels compared to the diesel-only operation. These products of the incomplete combustion consist up to 90% of methane [3], being a major greenhouse gas pollutant. Several studies have shown the potential of increasing the injection duration to mitigate UHC emissions as well as to improve the thermal efficiency [3,4,10,23]. However, such an approach leads to substantially increased soot and NO_x emissions [3,6,8,9]. This tradeoff clearly motivates further studies of improved engine geometries and advanced engine control systems and elucidates the need for improved fundamental and phenomenological understanding of the combustion as well as emissions formation processes in dual-fuel engines.

Dual-fuel combustion of the pilot-fuel in a lean natural gas mixture is a highly complex process involving short transient pilot fuel injection into the premixed gaseous fuel charge, pilot-fuel autoignition, combustion mode transition, and premixed flame propagation. A conceptual description of the dual-fuel combustion by three overlapping heat release sources was proposed by Karim [24]. First, the rapid combustion of the premixed pilot-fuel occurs. During the second and third stage, the gaseous fuel in the immediate vicinity of the ignition locations within the pilot fuel spray is burnt, followed by combustion of the premixed fuel by turbulent flame propagation. Several optical, numerical and engine studies addressed the influence of methane on the ignition delay and reported the strong inhibiting effect on ignition through chemical interaction [17,21,22,25–28]. More specifically, the low-temperature reactivity in pilot-fuel lean regions is considerably retarded leading to an overall increased ignition delay and lower pilot-fuel mixture reactivity. Nevertheless, little is known about the influence of methane on the processes after ignition. While the premixed flame is well understood from the spark ignited engines research and was studied even in the context of dual-fuel engines [15,29], the transition behavior of the pilot-fuel auto-ignition before established flame propagation has been rarely described in the literature. Only the recent work by Rochussen et al. [29] investigated the rate of burnt zone growth in an optically accessible dual-fuel engine. Recent work by Soriano et al. [30,31] investigated the dual-fuel combustion transition numerically.

In the context of this work, the transition phase of combustion is considered to be the interval from ignition until the time instant when the HRR is dominated by the premixed fuel combustion. It is understood from the optical studies that the transition-phase strongly influences the shape of the premixed combustion flame front (toroidal, radial) as well as the time instant and the flame surface area when premixed flame onsets [32]. Some engine studies studied the transition phase phenomenology by the HRR analysis [33]. Nevertheless, in engines, the HRR from the transition phase is masked by the rapid premixed flame propagation, thus making it challenging to extract information of the pilot-fuel combustion phase without the application of advanced optical diagnostics. Therefore, to correctly reproduce the experimental observations, the present phenomenological models of dual-fuel combustion strongly rely on several assumptions and parameter tuning.

Understanding the transition phase in the context of reactivity-controlled compression ignition (RCCI) combustion concept is more advanced [34–38]. This combustion concept utilizes two liquid fuels with different reactivity (autoignition characteristics) which are blended in the combustion chamber to generate a non-uniformity regarding the mixture auto-ignition characteristics. By quantifying the stratification of high-reactivity fuel, it was shown that the combustion proceeds via an auto-igniting flame front following the reactivity gradients. The auto-ignition of least reactive mixtures is accelerated through compression heating by the burnt gases. Therefore, the combustion duration and peak pressure rise rates are directly governed by the stratification of ignition time [34].

The scope of this study is to investigate the dual-fuel combustion transition phase from the pilot-fuel ignition until the premixed flame is established. Hereby, two distinct characteristics are particularly different from the RCCI combustion using liquid fuels: first, the chemical interaction of the premixed methane considerably changes the reactivity of the pilot-fuel, and second, the existence of the premixed flame. The transition phase, coupling ignition to the premixed flame propagation, strongly influences the shape of the established premixed flame and therefore strongly influences the combustion duration.

This publication (Part 1) investigates the phenomenology of the heat-release rate characteristics and its relation to the fuel-stratification prior to ignition. The heat-release rate (HRR), in the time interval between ignition and established premixed fuel HRR, was analyzed by defining combustion metrics (duration, peak, total energy) in order to characterize the combustion transition process. The HRR analysis has been supplemented by quantitative tracer-PLIF measurements to assess the pilot-fuel mixing distribution prior to ignition. A comprehensive matrix of measurements including variations of charge temperature at injection, charge oxygen content, premixed methane equivalence ratio, pilot injection duration and pressure, including several cross-variations, was acquired.

This publication is structured as follows: First, the experimental test rig and the HRR analysis procedure with the definition of HRR metrics are presented. The results section emphasizes the influence of charge and combustion parameters on the HRR metrics like ignition delay, pilot-fuel combustion duration, and peak-HRR. Finally, correlations of different combustion parameters are discussed while the experimental results corroborate the conclusions in regard to the parameter influence on the combustion during pilot-fuel burning.

Part 2 of this work will focus on improving the understanding of the underlying processes governing the transition. For this purpose, the combustion process was investigated using high-fidelity optical diagnostics (CH_2O-PLIF, Schlieren, OH*), supported with homogeneous-reactor and laminar flame speed simulations.

2. Experimental setup

2.1. Rapid compression expansion machine

A Rapid Compression Expansion Machine (RCEM) was utilized to compress the homogeneous methane/air charge in order to achieve engine relevant conditions at the time of pilot-fuel injection. This RCEM is a generic free-floating piston test rig (bore: 84 mm, variable stroke: 120–249 mm) with optical accessibility through piston and cylinder head windows. A brief description of the machine and its operation principle is provided here, while further descriptions are available in [19,21,39].

The machine operates in a single cycle mode (compression and partial expansion). The drive energy for the piston motion is provided through the compressed air charge acting on the RCEM working piston. The piston is not mechanically coupled to a flywheel – the piston acceleration is governed by the pressure difference between the driving volume and combustion chamber. In the cycle, first the driving volume

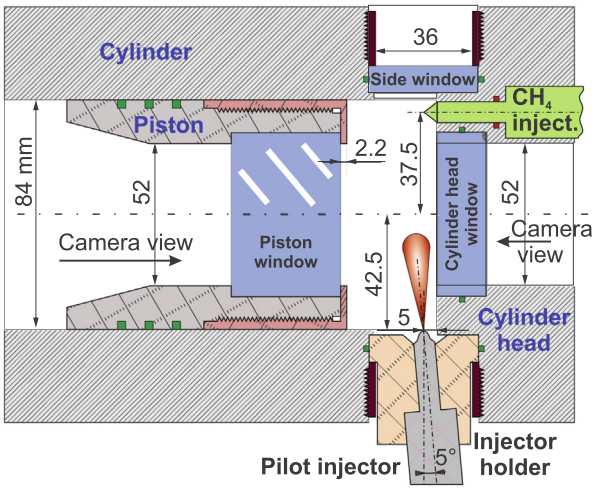

Fig. 1. RCEM combustion chamber geometry. Dimensions in mm.

is pressurized. Afterwards, the combustion chamber is filled to the desired bottom dead center (BDC) pressure. After the inlet valve is closed, methane is added using an injector as described below. After the set time allowed for mixing of methane with the charge, the rapid compression is initiated by releasing the coupling between the driving volume and piston. The subsequent piston motion resembles a pendulum-like swing with a fast ejection of the piston towards the top dead center (TDC). The piston decelerates as the driving volume pressure reduces and the pressure in the combustion chamber builds up, and afterwards swings back towards the equilibrium position. After the piston stops in the equilibrium position, the exhaust valve is opened to release the combustion chamber contents.

The RCEM combustion chamber has a cylindrical geometry with a flat cylinder head and virtually flat piston (2.2 mm piston bowl, Fig. 1). A standard common-rail diesel injector body (Bosch CRI2-16) equipped with a custom 100 µm diameter single-hole conical coaxial nozzle tip (KS 1.5, discharge coefficient C_d = 0.80) was used to admit the pilot fuel. The injector was mounted on the cylinder periphery at 5° axis inclination towards the piston, with the nozzle orifice located at a distance of 5 mm from the cylinder head and 42.5 mm from the cylinder axis.

Boundary conditions in this RCEM are precisely controlled and were investigated in previous studies. The charge temperature in the BDC is controlled with a multi-zone electric heating system of the cylinder walls and cylinder head. BDC temperature homogeneity better than σ = 3 K can be achieved [19]. Methane is admitted directly into the combustion chamber using a hollow-cone injector (Continental) – the injected quantity is controlled by adjusting the injector opening time (22–45 ms). Sufficient time for mixing with air (4 s) is allowed before compression is initiated. Methane mixture homogeneity in the present configuration was tested in [21] using tracer-PLIF method – the standard deviation of methane mixture σ = 6.7% was reported.

Despite the engine-like geometry, the flow field in this RCEM is not able to resemble the actual (turbulent) conditions found in engines. PIV investigation of the flow field during the compression reported quiescent conditions throughout the cycle [39]. No engine-like turbulence-generating features like the valve flow during the intake stroke or the squish motion in the piston bowl are present this RCEM combustion chamber.

The RCEM instrumentation enables a precise recording of the piston position (resolution 0.02 mm) and cylinder pressure (flush-mounted piezoelectric transducer, Kistler 7061B, 0–250 bar) at a rate of 100 kHz. The piezoelectric sensor is pegged using a precise absolute pressure transducer (Kistler 4075A10, 0–10 bar) in a fast-switching adapter (Kistler 741A). General RCEM specifications are given in Table 1.

Table 1
General specifications of the RCEM.

Cylinder bore	84 mm
Stroke	Adjustable, 120–249 mm
Displaced volume	0.67–1.38 dm^3
Realizable compression ratio	5–25
Charge intake pressure	1.1–2 bar
Cylinder head geometry	Flat
Piston bowl geometry	Top hat, Ø52 mm × 2.2 mm
Cylinder liner and head heating	Multi-zone electric, up to 450 K
Optical access	Piston window, Ø52 mm Cylinder head window Ø52 mm Lateral window Ø36 mm
Pilot fuel injection	Bosch CRI2-16 injector body Ø100 µm KS1.5 single hole coaxial nozzle Discharge coeff. C_d = 0.80 Steady mass flow rate: • 2.36 mg/ms (p_{inj} = 600 bar) • 3.33 mg/ms (p_{inj} = 1000 bar)
Methane injector	Continental outwards opening hollow-cone nozzle

2.2. Experimental conditions

In this study, the RCEM was operated at the maximal BDC displacement setting (1.38 dm^3 displacement, 249 mm BDC clearance to the cylinder head) to have a sufficient TDC clearance for minimizing the pilot spray interaction with walls.

The free-floating piston design of the machine results in an inherently uncertain piston motion which will be influenced by the combustion pressure rise, variation in the driving gas pressure, and friction of the piston motion. The operation strategy was selected based on preparatory studies. High compression ratio and early pilot injection before the TDC were selected to ensure a high repeatability of the conditions at SOI and to extend the operational range of the machine with respect to the maximal charge equivalence ratio. Fig. 2 shows the piston position, cylinder pressure trace, and estimated bulk temperature, along with an indication of SOI to demonstrate the RCEM operation strategy. The cylinder charge bulk temperature evolution was estimated using a thermodynamic model accounting for compression, wall heat losses, crevice volumes, and piston rings blow-by, as explained in more detail in section Appendix B.

The pilot fuel injection was triggered based on the pressure signal. A threshold of 25 bar was selected leading to SOI approximately 3.5 ms before TDC. The experimental matrix consists of three variations of experimental parameters as summarized in Table 2. First, a variation of the injection duration (ET variation) at 600 bar injection pressure was acquired at three different temperatures at the start of injection (T_{SOI}):

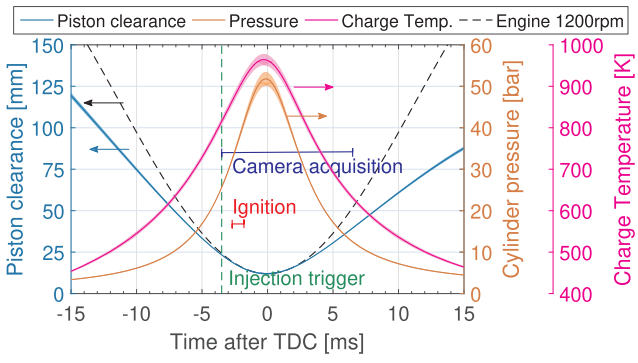

Fig. 2. Piston position, in-cylinder pressure trace, and charge temperature evolution averaged over 100 non-reactive cycles. 1 × σ variability of traces is demonstrated by the shaded regions. Stroke of an engine running at 1200 RPM is shown with the gray dashed line for reference. Injection timing is marked with a green line. (For interpretation of the references to color in this figure legend, the reader is referred to the web version of this article.)

Table 2
Overview of the operating conditions. Values in the 2nd row relate to the variation of T_{SOI} and ET, values in the 3rd row describe the variation of the P_{inj} and values in the 4th row show the EGR cases (reduced oxygen content). The parameters varied in each column are printed bold.

	T_{SOI}/ET variation	P_{inj} variation	EGR variation [O_2]
BDC displacement		1.38 dm^3	
Charge intake pressure		1.2 bar	
Stroke		236.5 mm ± 1 mm	
Compression ratio		20	
Max. piston speed		**9.0 m/s (piston position: 93 mm bTDC, time: 12 ms bTDC)**	
Pressure at SOI (P_{SOI})		25 bar	
BDC temperature	343, 363, 383 K		363, 383 K
Temperature at SOI (T_{SOI})	775, 810, 850 K		810, 850 K
Pilot injector energizing time (ET)	300, 400, 500 µs	300 µs	400 µs
Pilot injection duration	0.40, 0.58, 0.77 ms	0.45 ms	0.58 ms
Pilot injection pressure	600 bar	1000 bar	600 bar
Injected pilot-fuel mass [mg]	0.64, 1.18, 1.81 mg	1.21 mg	1.18 mg
Charge oxygen content % [O_2]	21	21	18, 15
Methane/air mixture equivalence ratio (φ_{CH4})	0, 0.33, 0.48, 0.53, 0.58, 0.66	0, 0.48, 0.53, 0.58	18% [O_2]: 0, 0.56, 0.62, 0.68 15% [O_2]: 0, 0.67, 0.74, 0.81
CH_4 injected mass	**0–64 mg**	**0–56 mg**	**0–56 mg**

775 K, 810 K, and 850 K, at the cylinder wall temperatures of 343 K, 363 K, and 383 K, respectively. The charge temperature in the BDC corresponds to the cylinder wall temperature. Hydraulic injection duration between 0.40 and 0.77 ms was considered. Second, a set of short (ET = 300 µs, hydraulic duration 0.45 ms) injections at higher injection pressure p_{inj} = 1000 bar was performed at the same range of T_{SOI}. The third variation investigates the influence of reduced oxygen content. Charge air was diluted with nitrogen resulting in a charge oxygen content of 18% or 15%. Injection pressure and ET were kept constant at p_{inj} = 600 bar and ET = 400 µs, respectively, and T_{SOI} of 810 K and 850 K were considered. The equivalence ratio of premixed fuel was varied in all considered cases.

The selected operation strategy with early injection ensures high repeatability of experimental condition during the ignition and combustion transition period. Nevertheless, it has to be noted that the thermodynamic conditions of the charge rapidly change (60 K/ms, Fig. 3). This leads to shorter ignition delays than if the conditions would remain steady after the SOI. Nevertheless, the observed trends when the T_{SOI} is changed remain valid since the relative differences in the charge temperature persist throughout the cycle (piston motion is independent of temperature).

The injection rate profile of the pilot injector was characterized for the selected rail pressures and energizing times using a “Bosch tube” type injection rate analyzer. The measured steady fuel injection rate at 30 bar tube pressure is 2.36 mg/ms and 3.33 mg/ms for 600 bar and 1000 bar rail pressure, respectively. The duration of the injector opening and closing transient is 140 µs (600 bar) and 110 µs (1000 bar), respectively.

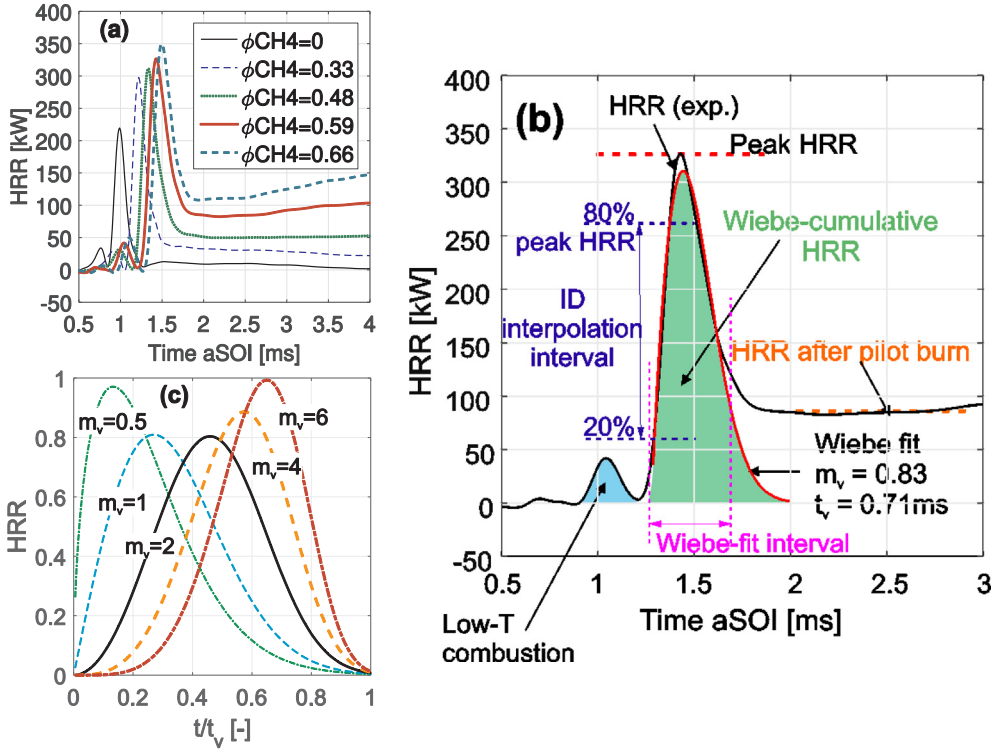

Fig. 3. (a) HRR curves for a variation of ϕ_{CH4} at T_{SOI} = 810 K, ET = 400 µs, (b) schematic of the HRR metrics, ID detection and Vibe fitting to the HRR, and (c) plot of the Wiebe-function shape for different values of the shape parameter m_v.

2.3. Definition of combustion metrics

The cylinder-charge bulk temperature evolution as well as the combustion heat release rate (HRR) were estimated using an in-house thermodynamic model accounting for compression, wall heat losses, crevice volumes and piston rings blow-by. Exact description of the HRR analysis and models is available in Appendix B. After the HRR has been calculated, the traces were processed to extract the combustion process relevant parameters.

A set of HRR metrics had to be defined to characterize the influence of different experimental parameters on the combustion HRR and transition from the pilot-fuel ignition until the premixed fuel combustion governs the HRR. These metrics were developed based on the characteristic shape of the HRR observed for all conditions. Here we focus primarily on the ignition behavior and transition between the pilot-fuel autoignition and HRR governed by the premixed fuel combustion. Throughout this time the flow field is governed by the pilot-jet induced turbulence. The premixed fuel combustion period is of secondary relevance – considerably different flame speeds are expected under the non-quiescent charge conditions found in engine applications. Furthermore, it cannot be distinguished from the HRR whether the premixed flame or entrainment of fuel into the burnt gases is responsible for the HRR after the pilot-fuel has been burnt.

Fig. 3a presents ensemble-averaged HRR curves (over 10 repetitions) for a variation of ϕ_{CH4}. The diesel-case ($\phi_{CH4} = 0$) HRR is characterized by two short peaks: the first small peak was attributed to low-temperature chemistry [26,34,40], followed by a larger peak during the second-stage ignition propagation through the pilot-fuel cloud. After the peak, only a small HRR is observed as the last fuel-rich regions leanout. In dual-fuel cases, the first stages of combustion proceed similarly as in the diesel-case – after the low-T chemistry a distinct peak HRR occurred during the auto-ignition of the pilot-fuel with entrained methane-air mixture. A higher peak HRR is observed for a higher ϕ_{CH4}. After the peak, a steep drop of HRR is observed and the HRR stabilizes as a premixed flame has established. The rate of change in HRR during the premixed flame propagation is much slower than during the pilot-fuel combustion.

First, the high-temperature ignition delay (ID) was determined based on the HRR, by fitting a tangent to the HRR during the rapid rise at ignition. The interval between 20% and 80% of the peak HRR value (demonstrated in Fig. 3b) was chosen to fit the tangent. The position on the time axis where this tangent intersects the abscissa was taken as the instant of the ignition. This procedure was found to be very robust, with low sensitivity of the detected ID to the selected thresholds of 20% and 80% for the tangent definition. In the second step, the HRR curves were ensemble averaged over 10 experimental repetitions. To reduce the smearing of the ensemble averaged $\overline{HRR}$ due to the small cyclic fluctuations of the ID, the HRR curves were shifted in time prior to the ensemble averaging for the difference between the average and single-shot ID ($ID_i - \overline{ID}$) as described by the equation: $\overline{HRR}(t) = \frac{1}{n} \bullet \sum_{i=1}^{n} HRR_i(t + (ID_i - \overline{ID}))$.

Based on the characteristic HRR shape (Fig. 3a), metrics of the HRR were derived as sketched in Fig. 3b. The pilot-combustion peak HRR (HRR_{pilot}^{MAX}) was evaluated as well as the HRR after pilot-fuel burned (averaged over the interval 0.6–1.5 ms after peak HRR). Additionally, the pilot-combustion duration and pilot-combustion cumulative HRR were evaluated based on the curve fitting over the peak HRR interval (denoted in magenta on Fig. 3b). The starting point of the interval was selected to be the ignition. Interval endpoint was determined as the time when HRR dropped below 20% of the difference between peak HRR and HRR after pilot burn. A functional form of the Wiebe function $\left(HRR \propto \frac{(m+1)}{t_v} \cdot \left(\frac{t}{t_v}\right)^m \cdot e^{-6.903 \cdot (t/t_v)^{m-1}}\right)$ was assumed – it can fit to various asymmetric bell-shaped peaks. Here, the t_v describes the function duration, and the shape parameter m_v determines the function shape, as demonstrated in Fig. 3c. In the present work, the Wiebe function shape was fitted to the above-described time interval using MATLAB nonlinear least squares fitting functionality. The function was found to well resemble the combustion HRR, both, with and without methane - a low uncertainty of the fitted parameters under all conditions can be reported. The highest uncertainty of the fit was in the value of m_v. This uncertainty propagates also into the less certain value of the curve width t_v. Nevertheless, the 95% confidence interval width calculated by the fit function was less than ± 8.5% of the t_v value under all investigated conditions. The confidence interval width of the pilot-combustion cumulative HRR remained below 11.7% of the value. The highest uncertainty of the fitted metric values is observed in cases with high ϕ_{CH4}, while the diesel cases have lower uncertainty. A detailed analysis of the metrics' uncertainties is provided in Appendix C.

The HRR metrics were extracted from the fitted Wiebe parameters as shown in Fig. 3c: t_v corresponds to the pilot combustion duration, and the area under the fitted curve as a metric for the pilot-combustion cumulative HRR. The shape parameter *m* determines the function shape and was not further analyzed as a metric by itself. The result of the fitting procedure is demonstrated in Fig. 3b.

It is emphasized that the t_v metric considerably exceeds any full-width at half-maximum Gaussian-deviation like metrics for combustion duration since it measures the time-interval from ignition until the fitted Wiebe function returns back to zero. Nevertheless, the so defined metrics enable a straightforward comparison over a wide range of conditions.

2.4. Optical investigation of pilot-fuel mixing evolution

To better understand the trends observed by the HRR analysis, the information on spray boundary conditions like the pilot-fuel mixture evolution and spray volume is of high value. The fuel distribution in case of short transient injections was shown to strongly depend on the end-of-injection transient with enhanced entrainment [41,42]. It also depends on the injector dynamics like the needle motion. The mass flow rate of injector used in the present study was characterized using a 'Bosch-tube' type analyzer. Nevertheless, to provide higher-fidelity information about the pilot mixing in the RCEM test-rig geometry, a dedicated set of experiments under non-reactive conditions was performed. For this purpose, quantitative tracer-PLIF, Mie scattering and Schlieren imaging were combined. Experimental details on the optical methods are provided in Appendix A. In this subsection the processing approach to derive combustion relevant spray metrics like the median and maximal pilot-fuel equivalence ratio and spray volume are introduced.

Tracer-PLIF was used to measure pilot-fuel equivalence ratio at a temporal resolution of 10 kHz. This measurement method provides two-dimensional cross-section images of the tracer-fluorescence from both the liquid and vapor phase. In the vapor phase, the signal was quantified as described in Appendix A. In the liquid phase, tracer-PLIF cannot be quantified. Therefore, the information from Mie-Scattering imaging was used to remove the liquid phase fluorescence from the PLIF images before the signal was quantified. In addition to tracer-PLIF and Mie-scattering imaging the high-speed Schlieren imaging was performed to provide temporally well-resolved information of the spray contour evolution.

Using the information from these optical methods, fuel-mixing metrics were derived. Maximal pilot-fuel equivalence ratio was evaluated, along with the mass-median equivalence ratio, defined as the equivalence ratio ϕ where half of the pilot-fuel mass is at higher ϕ. This data was ensemble-averaged from 10 experimental repetitions. In addition, the spray volume was estimated from the Schlieren spray contours. Axial symmetry was assumed to derive the spray volume from the 2-dimensional spray contour information. The information of the spray volume opens the possibility to extract yet another metric, the average pilot-fuel density within the spray. This was defined as the total injected fuel mass divided by the spray volume.

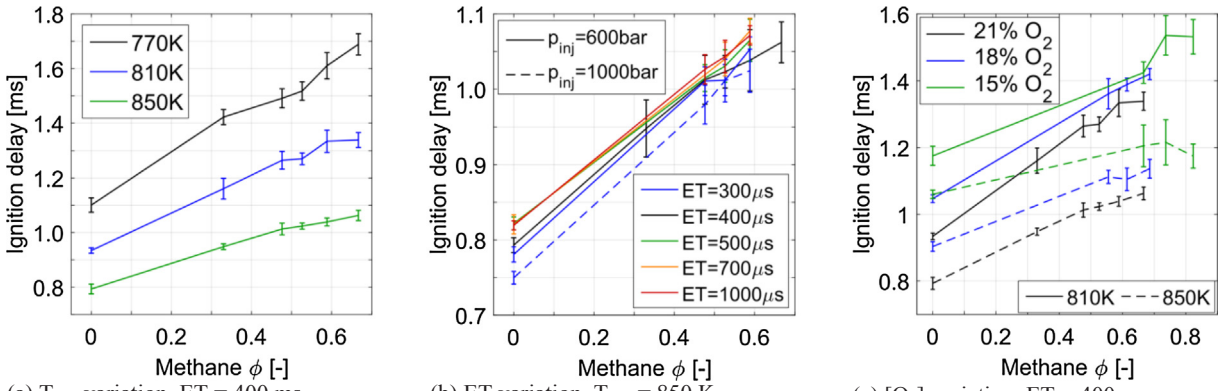

(a) T_{SOI} variation, ET = 400 ms (b) ET variation, T_{SOI} = 850 K (c) [O_2] variation, ET = 400 µs

Fig. 4. Influence of charge methane ϕ_{CH4} on the pilot-fuel ignition delay for a variation of T_{SOI} (a), injection ET (b) and charge oxygen content (c). Error bars indicate the standard deviation of the detected ID times.

The investigations were performed using dodecane as a surrogate fuel for the diesel fuels used in dual-fuel engines. The thermophysical properties of n-dodecane are very close to the properties of commercial diesel fuels. Therefore, it is expected that the mixing trends reported in this section remain valid also in the case of commercial fuels [43,44].

3. Results

3.1. Influence of methane on the pilot-fuel ignition delay

The ignition delays (ID) were determined based on the tangent fitting to HRR as described in Section 2.3. Fig. 4 presents the influence of premixed methane equivalence ratio (ϕ_{CH4}) on ID for a wide variation of experimental conditions: (a) variation of T_{SOI}, (b) variation of injection ET, and (c) variation of charge oxygen content [O_2].

For all investigated conditions the addition of methane was found to strongly delay the pilot fuel ignition. At all investigated T_{SOI} while keeping the injection parameters constant, a monotonous increase of ID for increasing ϕ_{CH4} was detected, with nearly linear dependence on ϕ_{CH4} (Fig. 4a). In addition, both the absolute and relative ID sensitivity to ϕ_{CH4} increased at lower T_{SOI}. Up to 55% increased ignition delay was observed under the highest considered ϕ_{CH4}. Similar influence was reported before in RCEMs [20,21,25,40] and optical engines [17]. Investigations in [25] showed that this is due to a chemical interaction of methane inhibiting the low-T ignition in lean pilot-fuel mixtures. Other methane influences like the change of T_{SOI} due to changed specific heat ratio, and lower oxygen concentration due to the dilution of air with methane, were shown to be negligible in comparison to the methane chemical effect.

Fig. 4b presents the dependence of ID on pilot injector ET and ϕ_{CH4} at T_{SOI} = 850 K. Additional measurements with ET of 700 and 1000 µs from [21] were added to include cases with the ignition delay shorter than the injection duration (negative ignition dwell time). A coherent trend of shorter injections exhibiting a shorter ignition delay was observed independently of methane concentration. The diesel-case ET = 300 µs injection at p_{inj} = 1000 bar showed 150 µs (17%) shorter ignition delay than the longer injections at p_{inj} = 600 bar. When increasing the injection duration beyond ET = 500 µs (ignition dwell approximately zero) no additional dependence of ID on the injection ET was observed. This indicates that this effect of shorter ID for shorter injections is driven by the end of injection entrainment wave [41] as already observed before in an optical engine by Malbec et al. [45]. In the present work, this effect is less pronounced than in [45]. For very short injections, on the other hand, a longer ignition delay would be expected due to the reduced reactivity of the available mixture, potentially also leading to misfire [46]. No such behavior has been observed in the present investigations even at T_{SOI} = 770 K conditions and highest considered ϕ_{CH4} (not shown here). This indicates that within the ignition delay range of 0.7–2.0 ms detected in this study the pilot-fuel concentration does not drop sufficiently to reach the misfire regime.

Finally, the combined influence of charge oxygen content [O_2] and ϕ_{CH4} on the ID has been investigated at T_{SOI} of 810 K and 850 K (Fig. 4c). Same concentrations of methane in the charge as for the 21% oxygen cases have been considered, leading to higher values of ϕ_{CH4} in the reduced [O_2] cases. About 30% increased ID at ϕ_{CH4} = 0 was measured at 15% [O_2] comparing to the 21% [O_2] cases, in good agreement with the relation ID $\propto$ [O2]$^{-1}$ from [47]. In the charges with reduced oxygen content, a lower sensitivity of ID to methane was detected than at 21% [O_2], resulting in an only moderate increase of ID in dual-fuel cases when reducing the [O_2]. The relation ID $\propto$ [O2]$^{-1}$ from [47] over-predicts the oxygen concentration effect on ID in dual-fuel cases.

3.2. Dependence of HRR on the pilot injection and charge conditions

Having demonstrated large influence of methane on ignition delay, in this section, we investigate the influence of methane concentration, injection parameters, and charge conditions on the HRR metrics: t_v, pilot-combustion peak HRR (HRR_{pilot}^{MAX}), and pilot-combustion cumulative HRR. Fig. 5 presents the dependence of HRR metrics on the T_{SOI} and ϕ_{CH4}. A considerable increase in t_v was observed under the dual-fuel conditions. Whereas in the diesel-cases similar value of t_v was observed for all T_{SOI}, a larger prolongation of the t_v with ϕ_{CH4} was measured for the colder charge conditions. The addition of methane also increases the HRR_{pilot}^{MAX} with, again, a stronger influence at lower T_{SOI}. Overall, in the diesel-case, the pilot-combustion cumulative HRR correlates well with the pilot-fuel LHV. With increasing ϕ_{CH4}, a considerable increase of the pilot-combustion cumulative HRR was observed: up to 5 times at ϕ_{CH4} = 0.66, T_{SOI} = 770 K. This indicates a considerable contribution of the entrained methane combustion to the total heat released during the transition and suggests the existence of regions with lean-mixture within the pilot-fuel spray cloud at the time of ignition. At higher T_{SOI} less of the entrained methane is combusted as explained by the shorter ID leading to pilot-fuel richer conditions at ignition. This strong sensitivity of all combustion metrics to methane appears to be lost at high ϕ_{CH4}. As shown by the width of the confidence bond (error bars), this loss of sensitivity might not be physically substantiated. Nevertheless, the general trend of increasing t_v and pilot-combustion cumulative HRR with ϕ_{CH4} is not questionable.

Fig. 6 shows the dependence of HRR metrics on the injection ET, p_{inj}, and ϕ_{CH4} at T_{SOI} = 810 K. For all pilot injections, prolonged duration t_v was observed with higher ϕ_{CH4}. The higher p_{inj} case (p_{inj} = 1000 bar, ET = 300 µs) showed the highest sensitivity to methane, whereas all injections at p_{inj} = 600 bar resulted in a comparable

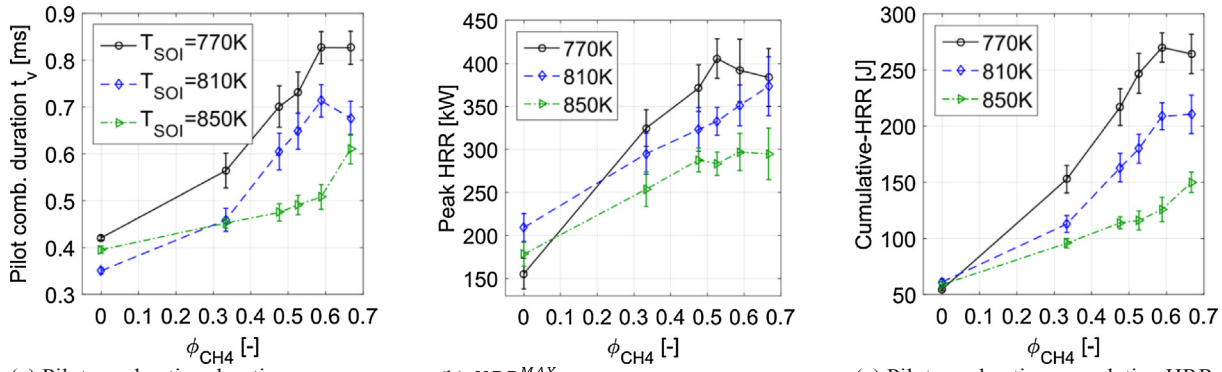

(a) Pilot-combustion duration (b) HRR_{pilot}^{MAX} (c) Pilot-combustion cumulative HRR

Fig. 5. Dependence of HRR metrics for a variation of T_{SOI}. Injection parameters: ET = 400 µs, p_{inj} = 600 bar. Error bars of t_v and pilot-combustion cumulative HRR present the 95% confidence bond of the metric, peak-HRR error bars the shot-to-shot standard deviation of the metric.

increase of t_v with increasing ϕ_{CH4}. Observing the HRR_{pilot}^{MAX} metric, a clear dependence of the HRR_{pilot}^{MAX} on the injected pilot-fuel mass (related to the ET) is visible. The results of the medium injection duration case (ET = 400 µs) and higher p_{inj} case (p_{inj} = 1000 bar) having a similar mass of the injected pilot-fuel and very similar HRR_{pilot}^{MAX} evolution thereby confirm this statement. For all injection variations, a comparable sensitivity of the HRR_{pilot}^{MAX} to ϕ_{CH4} was observed. Similarly to the dependence of HRR_{pilot}^{MAX} on the injected mass, such dependence has been also detected in the pilot-combustion cumulative HRR metric. Nevertheless, the curve for the ET = 400 µs injection is less steep than for the shorter p_{inj} = 1000 bar injection with similar injected mass. This was attributed to a faster entrainment of methane at the higher injection pressure.

Last, we investigate the influence of reduced charge oxygen content [O_2] and variable ϕ_{CH4} on the HRR metrics at T_{SOI} of 810 K. Points acquired at 850 K are shown as well to compensate for the [O_2] effect on ID (Fig. 7). In all cases, a very strong prolongation of t_v has been recognized with reduced [O_2] and high ϕ_{CH4} regardless of the ID and T_{SOI}. This indicates a strong reduction of the overall reactivity in the cases combining methane and reduced [O_2]. In a comparison of T_{SOI} = 810 K case at 21% [O_2] and 850 K case at 15% [O2], the colder 21% [O2] case shows a considerably shorter t_v at a comparable ID (Fig. 5a). This increase of the t_v at reduced [O_2] exhibits itself also in a remarkably reduced HRR_{pilot}^{MAX}. At ϕ_{CH4} = 0, around 30% reduced HRR_{pilot}^{MAX} is observed at 15% [O_2] relative to the 21% case, as also expected from studies of EGR in diesel combustion [48]. Whereas for all 21% [O_2] cases a clear trend of a higher HRR_{pilot}^{MAX} with increasing ϕ_{CH4} has been observed, this trend is less pronounced for the 18% [O_2] cases and even inverted in the 15% [O_2] cases. In terms of the pilot-combustion cumulative HRR, a lower value of this metric has been recognized with reducing the O_2. Nevertheless, the trend of increasing cumulative HRR is present even in the 15% [O_2] case, though less pronounced. Oxygen appears not to be the reactant limiting the HRR_{pilot}^{MAX}. This indicates a chemical effect of combined methane and reduced [O_2] content, increasing the t_v and decreasing the HRR_{pilot}^{MAX}.

3.3. Pilot-fuel mixing state evolution

To better understand the above-observed trends, the information on spray boundary conditions like the pilot-fuel mixture evolution and spray volume is of high value. Fig. 8 draws the temporal evolution of maximal and mass-median (half of the pilot-fuel mass at higher ϕ) dodecane/air equivalence ratio (ϕ_{C12}) extracted from 10 experimental repetitions at all considered injection pressures and ET. During the pilot-fuel injection the measurements indicate very high maximal ϕ_{C12}. After the end of injection (EOI), maximal and mass-median ϕ_{C12} rapidly decrease. As expected due to a later EOI, the longer pilot-injections show a longer persistence of the rich-zones. Throughout the cycle, the value of maximal ϕ_{C12} is approximately a factor 2 higher than the mass-median value. It is interesting to note that both ET = 300 µs injections (at 600 bar or 1000 bar injection pressure) show a very similar evolution of both the maximal and the mass-median ϕ_{C12}, despite a factor 2 difference in the injected mass.

Besides the mass-median pilot-fuel equivalence ratio, the fuel-jet volume and average pilot-fuel density (pilot-fuel mass divided by the spray volume) were selected as the meaningful values describing the pilot-fuel jet state, and were used to investigate correlations of pilot-fuel mixing state to the HRR metrics shown in the section "Discussion". The volume of the spray was derived from the processed Schlieren images under an assumption of spray axial symmetry (Section 2.4 and Appendix A). The average fuel density was calculated as the injected

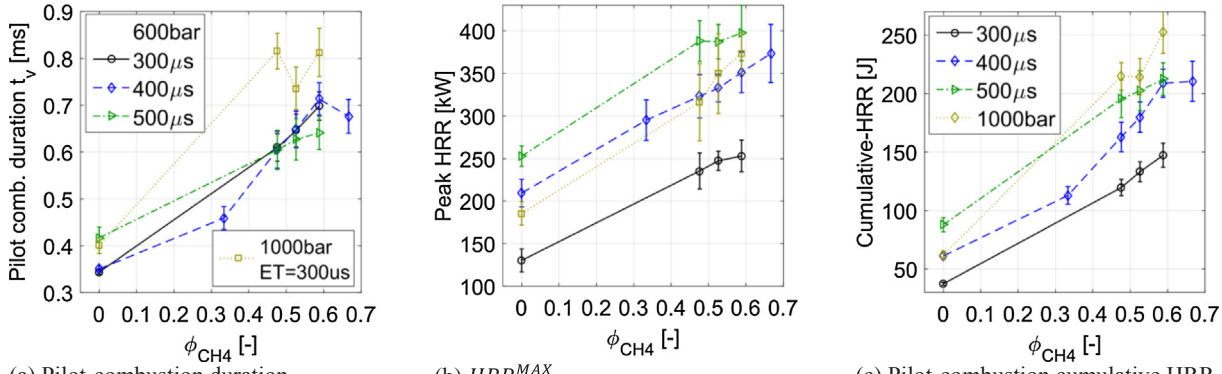

(a) Pilot-combustion duration (b) HRR_{pilot}^{MAX} (c) Pilot-combustion cumulative HRR

Fig. 6. Dependence of HRR metrics for a variation of injection ET and p_{inj} at T_{SOI} = 810 K. Error bars of t_v and pilot-combustion cumulative HRR present the 95% confidence bond of the metric, peak-HRR error bars the shot-to-shot standard deviation of the metric.

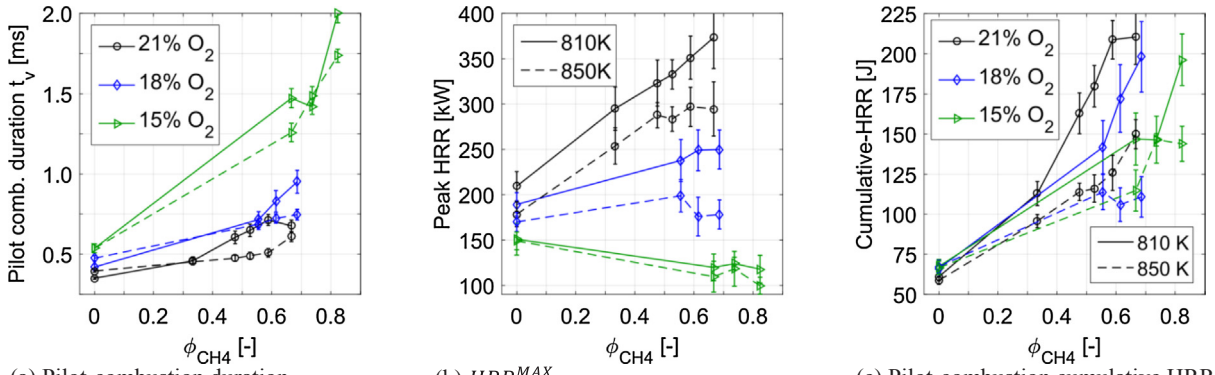

(a) Pilot-combustion duration (b) HRR_{pilot}^{MAX} (c) Pilot-combustion cumulative HRR

Fig. 7. Dependence of HRR metrics for a variation charge oxygen content. Injection parameters: ET = 400 µs, p_{inj} = 600 bar. Error bars of t_v and pilot-combustion cumulative HRR present the 95% confidence bond of the metric, peak-HRR error bars the shot-to-shot standard deviation of the metric.

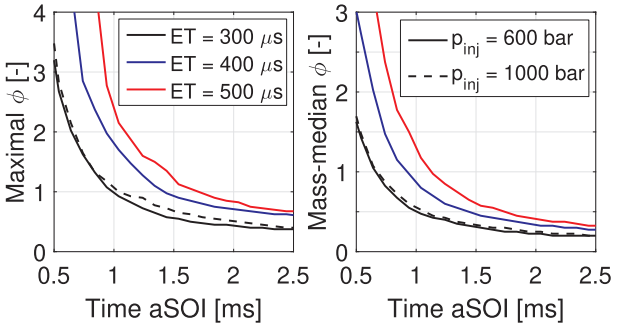

Fig. 8. Temporal evolution of maximal (left) and fuel-mass median (right) pilot-fuel equivalence ratio for a variation of injector ET and p_{inj}.

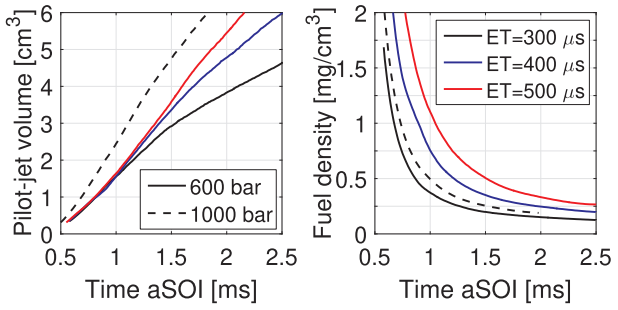

Fig. 9. Evolution of pilot-spray plume volume (left) and pilot-fuel density (right) for a variation of injector ET and p_{inj}.

mass of fuel divided by the fuel-jet volume. Fig. 9 presents the evolution of pilot-spray plume volume and averaged fuel density for all considered pilot injections.

The high-pressure injection initiates the highest spray-volume, followed by the injections at p_{inj} = 600 bar in the order of decreasing ET. Rather low influence of ET at p_{inj} = 600 bar up to 1.4 ms aSOI has been observed. Similar predictions are calculated also by the 1-D spray models, which suggest no deviation of spray penetration from the penetration of an infinite injection case, up to twice the injection duration [41]. Overall, this leads to considerable influence of injection duration on the average fuel-density, with longer injections leading to a higher fuel density (Fig. 9). In the terms of fuel-density the 1000 bar injection lies between the 300 µs and 400 µs ET injections at p_{inj} = 600 bar. The tracer-PLIF investigations confirm a similar evolution of the median equivalence ratio as predicted by the schlieren-based fuel-density estimation (Fig. 8, right).

4. Discussion

Results show that combustion parameters like T_{SOI}, ϕ_{CH4}, injector ET, p_{inj} and [O_2] strongly influence the HRR metrics like the t_v and pilot-combustion peak-HRR (HRR_{pilot}^{MAX}). Furthermore, these parameters simultaneously influence boundary conditions like the ID, flow field at ignition, and pilot-fuel mixing. Thus, identifying the governing processes is challenging. However, several mechanisms were identified as major drivers influencing the transition:

- Chemical influence of methane changing the pilot-fuel mixture reactivity
- Injection-induced turbulence and its decay
- Pilot-fuel mixing state at ignition, related to the pilot-fuel reactivity at this state
- Diffusion-combustion at the interface between the fuel-rich burnt pilot-fuel-jet and surrounding charge
- Availability of oxygen in the pilot-jet

The discussion attempts to corroborate the results from the complete experimental matrix in order to identify the first-order influences on dual-fuel combustion during the transition from ignition until the premixed fuel combustion governs the HRR. The HRR metrics of the whole measurement matrix were correlated to parameters like ignition delay, pilot-fuel mixing field, or pilot-fuel stratification. The analysis of influences in the cases with reduced oxygen content is presented separately.

4.1. HRR metrics correlation to the ignition delay

In the framework of this work, the reactivity of a mixture is understood to be related to the mixture ignition characteristics (higher reactivity leading to a shorter ID). As discussed above the reactivity of dodecane in a methane/air mixture depends on both T_{SOI} and ϕ_{CH4}. Fig. 10 presents the correlation of HRR metrics t_v and HRR_{pilot}^{MAX} to the pilot-fuel ID with the aim to investigate the coupling between the global 'highest reactivity' (represented by the ID) and the overall mixture reactivity (related reactivity stratification within the pilot jet) represented by the t_v or HRR_{pilot}^{MAX}.

A consistent trend of increasing duration of pilot-fuel combustion t_v with the increasing ID is visible in Fig. 10 left. Nevertheless, significant differences among diesel and dual-fuel cases, and among the cases with different injection parameters were observed. The diesel-cases show a rather short ID as well as t_v independent of the T_{SOI}. Exceptions are the ET = 300 µs injections at T_{SOI} = 770 K, representing the least-reactive diesel-cases of the matrix, showing longer t_v. In dual-fuel cases, the t_v is more sensitive to ϕ_{CH4} than to ID. Starting the analysis at 770 K T_{SOI}: a considerable decrease of the t_v with increasing injection duration has

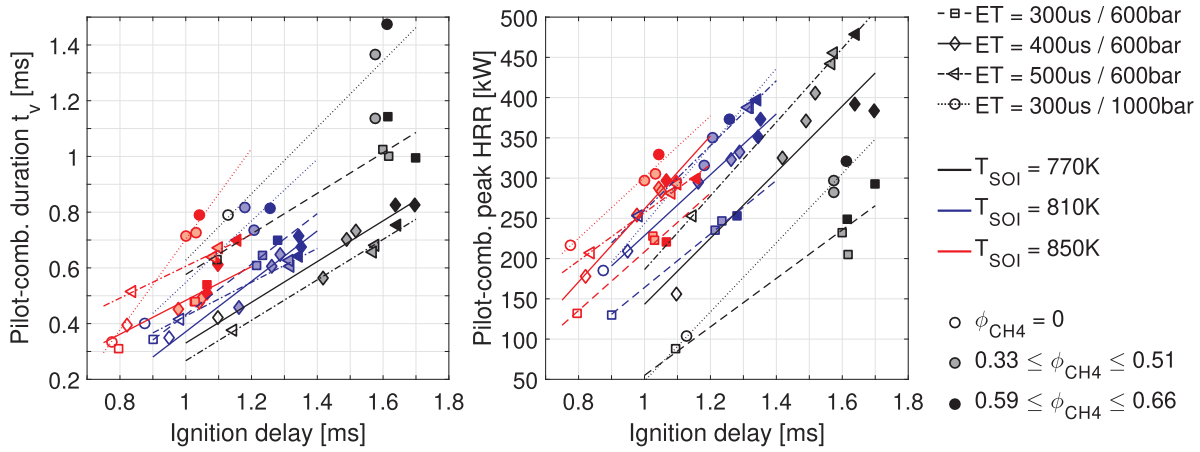

Fig. 10. Correlation of pilot combustion duration tv to ignition delay (left) and correlation of the HRR_{pilot}^{MAX} pilot-combustion to the ignition delay (right). Marker shape indicates the pilot injection parameters, marker color the T_{SOI}, and marker fill the ϕ_{CH4}, according to the legend. Lines are linear fits to the ϕ_{CH4} variation data-points at otherwise same conditions.

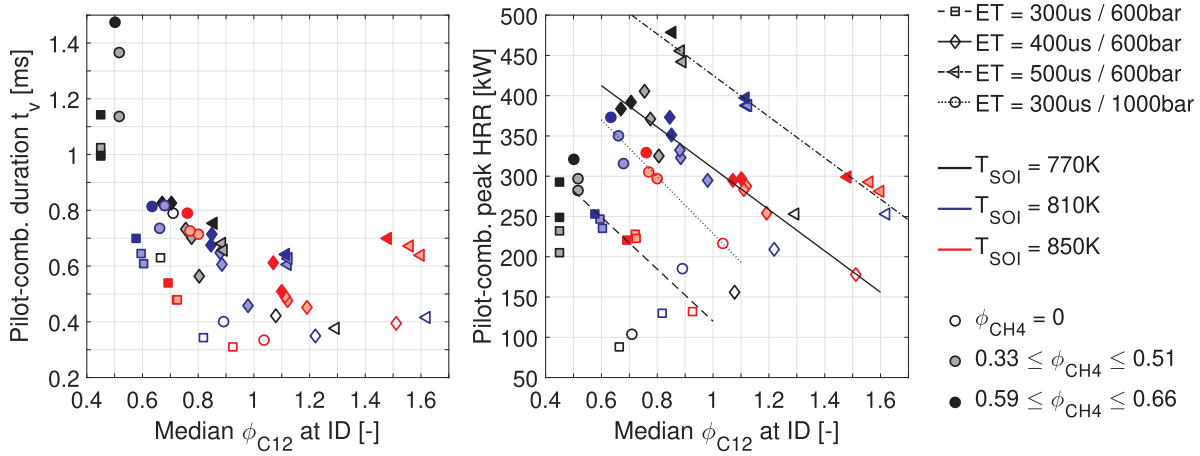

Fig. 11. Correlation of t_v (left) and HRR_{pilot}^{MAX} pilot-combustion (right) to the median equivalence ratio ϕ_{C12} at the time of ignition. Marker shape indicates the pilot injection, marker color the T_{SOI}, and marker fill the ϕ_{CH4}, according to the legend.

been observed. Nevertheless, a similar absolute sensitivity of t_v on ID (and ϕ_{CH4}) has been observed for all points at p_{inj} = 600 bar. A higher sensitivity has been observed for the p_{inj} = 1000 bar injection. The faster pilot-fuel combustion for longer injections is explained mostly by the fuel-richer conditions available at the time of ignition. The increased sensitivity of t_v to ϕ_{CH4} at p_{inj} = 1000 bar cannot be directly explained by this argument. This will be further discussed in Sections 4.2 and 4.3. By increasing the T_{SOI}, the differences among different injection-duration cases diminish and the influence of ET on the t_v becomes ambiguous: t_v of the ET = 500 µs injection becomes longer than for the shorter injections at T_{SOI} = 850 K. This is explained here by the considerable portion of pilot-fuel located in fuel-rich zones: the diffusion combustion at the stoichiometric contour leads to HRR after the pilot-fuel has burnt. In general, t_v appears to be only weakly coupled to the ID in the dual-fuel cases – a significantly stronger influence of ϕ_{CH4} on t_v has been observed.

Investigating the correlation of HRR_{pilot}^{MAX} to the ID (Fig. 10 right), a general tendency of a higher HRR_{pilot}^{MAX} with increased T_{SOI} and in cases with higher injected pilot-fuel mass was observed. The influence of pilot-fuel mass is straightforward: a larger amount of combustible mixture available at the time of ignition as well as larger spray volume at ignition lead to higher HRR_{pilot}^{MAX} values. Methane effect on ID explains the trend of higher HRR_{pilot}^{MAX} with increasing the T_{SOI}: to maintain the ID with increasing ϕ_{CH4}, the T_{SOI} has to be increased. Therefore, additional methane is mixed into the pilot-fuel at an otherwise unchanged pilot-fuel mixture – this leads to higher HRR_{pilot}^{MAX}. The pilot injection-pressure influence is interesting: High-pressure injection admits a comparable pilot-fuel mass as the ET = 400 µs injection at p_{inj} = 600 bar. Nevertheless, at T_{SOI} = 770 K, in comparison to the ET = 400 µs injection, a significantly lower HRR_{pilot}^{MAX} is observed at p_{inj} = 1000 bar. Considering t_v prolonged by a factor of 2, this is expected due to the overall comparable available energy within the pilot-fuel jet. Contrary, at higher T_{SOI}, the high-pressure injection shows the highest HRR_{pilot}^{MAX}. This is explained by the oxygen availability limiting the HRR_{pilot}^{MAX} in cases with a longer ET and low injection pressure.

Apart from the increased t_v along with the decreased HRR_{pilot}^{MAX} at low T_{SOI} dual-fuel cases, no other indication of lean-out or misfire has been observed: in all cases, the HRR_{pilot}^{MAX} increased with the addition of methane regardless of the longer ID and prolonged t_v.

4.2. HRR metrics correlation to the pilot-fuel mixing field

Tracer-PLIF data (Section 2.4 and Appendix A) providing information on the mixing field of pilot-fuel at the time of ignition was used to understand the influence of pilot-fuel mixing on combustion metrics. The correlations of t_v and HRR_{pilot}^{MAX} in regard to the mass-median ϕ_{C12} are presented in Fig. 11.

A clear tendency of extended t_v under leaner pilot-fuel conditions (lower mass-median ϕ_{C12}) is visible from Fig. 11 (left). In the diesel-cases (empty symbols), a minimum of t_v is apparent at a mass-median

ϕ_{C12} around stoichiometry. Longer transition time in leaner cases can be attributed to the large portion of fuel-mass located under lean conditions, under which the mixture is less reactive. The dual-fuel cases follow a similar trend of a longer t_v with leaner ϕ_{C12} as in the diesel-cases – confirming the strong influence of pilot-fuel mixing state on the combustion transition. Generally, with increasing ϕ_{CH4}, a longer t_v at same ϕ_{C12} has been observed. This was expected due to the chemical influence of methane on the autoignition of lean ϕ_{C12} [25].

The correlation of HRR_{pilot}^{MAX} to ϕ_{C12} shows a strong influence of both, ϕ_{C12} and pilot-injection strategy, on the HRR_{pilot}^{MAX} (Fig. 11 right). Investigating the diesel-cases first, we see a higher HRR_{pilot}^{MAX} with higher ϕ_{C12}, which is primarily the influence of a positive correlation between mean ϕ_{C12} and pilot-fuel mass injected. Additionally, especially at low T_{SOI}, the higher reactivity of richer ϕ_{C12} mixture contributes to the increasing HRR_{pilot}^{MAX}. Dual-fuel cases using same pilot-injection settings show a clear correlation of HRR_{pilot}^{MAX} to the ϕ_{C12} at ignition: an almost linear increase of the HRR_{pilot}^{MAX} with decreasing ϕ_{C12} was observed regardless of the T_{SOI} and ϕ_{CH4}. This is demonstrated by the fitted lines on Fig. 11b. Only the diesel-cases and the cases with very long ID show a deviation from this behavior. A larger amount of entrained methane can be combusted at decreased ϕ_{C12} (same pilot-fuel mass) due to the overall decreased total equivalence ratio. Considering the moderate influence of CH_4 on t_v, a higher quantity of entrained methane is evident in higher HRR_{pilot}^{MAX}. The same trend was observed also for the high p_{inj} case. Nevertheless, lower HRR_{pilot}^{MAX} values than for the ET = 400 µs case were observed at same ϕ_{C12} despite the comparable injected mass. The stratification and local distribution of the pilot-fuel within the spray might be responsible for the observed differences.

To investigate the effect of local fuel distribution, the correlation of t_v and HRR_{pilot}^{MAX} to the spray-plume volume at the time of ignition, as a measure of fuel stratification, is presented in Fig. 12. Similarly, as observed in the correlations of t_v and ϕ_{C12}, a weak correlation between increasing t_v and increasing pilot-spray plume was observed. Only the short T_{SOI} = 770 K injections are clear outliers and were already identified above to be on the edge of leaning-out.

Correlation of HRR_{pilot}^{MAX} and jet-volume shows a clear upper-bound of HRR_{pilot}^{MAX} also marked by the straight line (Fig. 13 right). Oxygen appears to be the limiting reactant on this upper line and the overall reactivity of the mixture plays a minor role. Only the short T_{SOI} = 770 K points and some diesel cases considerably deviate from this upper bound. These deviating points were already identified to be close to lean-out indicating very lean conditions at ignition, where the oxygen-limit does not apply anymore.

4.3. Influence of reduced charge oxygen content

The reduced oxygen content cases simulate a reduced charge reactivity as achieved with use of EGR in real engines. Considerably prolonged ignition delay, prolonged t_v, and reduced HRR_{pilot}^{MAX} were reported in Sections 3.1 and 3.2. Fig. 13 shows the dependence of t_v and HRR_{pilot}^{MAX} on the ignition delay for a variation of $[O_2]$ and T_{SOI}. The aim of this variation is to distinguish the influence of reduced $[O_2]$ on the ignition delay and mixture reactivity after ignition.

Correlation of t_v and ID again shows a very strong $[O_2]$ influence leading to a significant reduction of the mixture reactivity (Fig. 13 left). T_{SOI} of 810 K and 850 K for injection setting ET = 400 µs and p_{inj} = 600 bar were considered. Comparing the 15% $[O_2]$ case at T_{SOI} = 850 K to the 21% $[O_2]$ case at both T_{SOI} = 770 K and 810 K, the strong influence of oxygen content is visible: while the ID and injector ET are comparable, by a factor of 2 higher values of t_v were detected despite the higher T_{SOI}. This shows a considerable reduction of chemical reactivity in the combined methane and reduced $[O_2]$ cases. This influence is significantly less pronounced in the 18% $[O_2]$ cases. Comparing the T_{SOI} = 810 K and T_{SOI} = 850 K cases, shorter t_v values were observed at lower T_{SOI}. A possible explanation is the overall very rich mixture due to the shorter ID at 850 K (ϕ_{CH4} up to 0.8 with reduced $[O_2]$ results in high overall equivalence ratio).

This strong influence of $[O_2]$ on t_v exhibits itself also in the decreased HRR_{pilot}^{MAX} (Fig. 13 right). Again, a considerably higher influence of $[O_2]$ on the HRR_{pilot}^{MAX} than on the ID is observed, especially pronounced at 15% $[O_2]$ case. The decreased influence of ϕ_{CH4} is partially attributed to oxygen being the limiting reactant. Nevertheless, this can lead to only up to a HRR_{pilot}^{MAX} decrease proportionally corresponding to the $[O_2]$ reduction. However, the observed reduction is significantly higher. This indicates the chemical influence of methane under reduced $[O_2]$ to be the dominant effect decreasing the HRR_{pilot}^{MAX}.

5. Summary and conclusions

Combustion of pilot-fuel in a compressed methane/air mixture was investigated in a rapid compression-expansion machine (RCEM), analogous to the combustion transition process from ignition until established premixed flame in pilot-ignited lean natural gas engines. The aim was to understand the influence of operation parameters on pilot-fuel burning: methane/air equivalence ratio, charge temperature, and oxygen content, as well as pilot-injection strategy, were varied. The quiescent flow field in the RCEM enabled studying of the pilot-fuel burning without the heat release rate (HRR) being masked by a rapid premixed flame spreading. HRR analysis was supplemented with non-

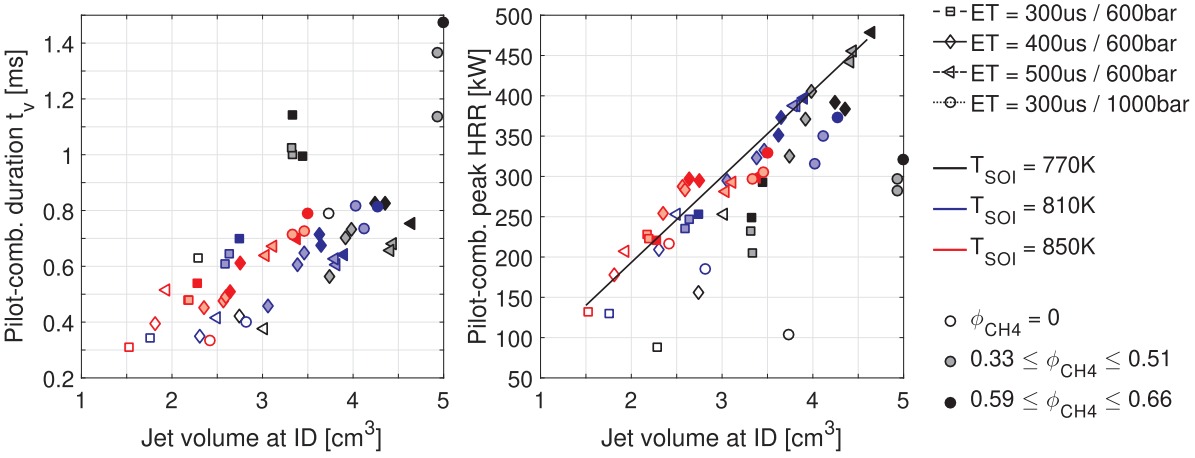

Fig. 12. Correlation of t_v (left) and pilot-combustion peak-HRR (HRR_{pilot}^{MAX},right) to the volume of the pilot-fuel jet at the time of ignition. Marker shape indicates the pilot injection strategy, marker color the T_{SOI}, and marker fill the ϕ_{CH4}, according to the legend. The black line on the right-plot was drawn manually to help visualize the upper-boundary of HRR_{pilot}^{MAX} values.

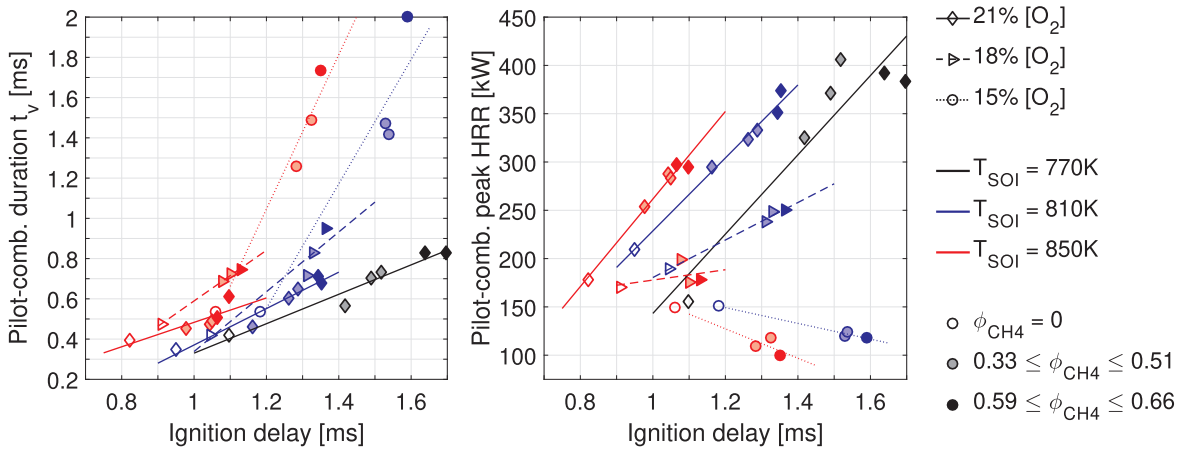

Fig. 13. Correlation of t_v (left) and HRR_{pilot}^{MAX} pilot-combustion (right) to the ID for a variation of charge oxygen content [O_2]. Marker shape indicates the charge oxygen content [O_2], marker color the T_{SOI}, and marker fill the ϕ_{CH4}, according to the legend. Conditions: ET = 400 µs, p_{inj} = 600 bar.

reactive Schlieren and tracer-PLIF optical data of the pilot-fuel spray penetration and average pilot-fuel mixture fraction. HRR metrics like pilot-fuel combustion duration t_v and pilot combustion peak-HRR (HRR_{pilot}^{MAX}) were determined. Correlations of different combustion metrics to the pilot-fuel injection and charge properties were investigated, in order to derive conclusions regarding the major influences on the transition from pilot-ignition until the premixed fuel combustion governs the HRR in pilot-ignited lean-premixed CNG engines.

Based on the analysis of experimental results the following conclusions can be stated:

1. Increasing methane amount leads to a longer pilot-fuel ignition delay. Higher absolute and relative sensitivity to methane has been observed at lower T_{SOI} and/or at reduced charge [O_2].
2. Pilot-injection parameters were found to have a small influence (up to 10%) on the ignition delay (ID) both in the diesel and dual-fuel cases. Nevertheless, a consistent trend of shorter injections having a shorter ignition delay was found and attributed to the end of injection entrainment wave influence in line with previous investigations in optical engines [45].
3. In the diesel-cases the shortest pilot combustion duration t_v was detected for cases with the median pilot-fuel equivalence ratio (ϕ_{C12}) at ignition around stoichiometry. Slower combustion at leaner conditions was attributed to the reduced mixture reactivity, and at fuel-richer conditions to the high contribution of pilot-fuel-mixing-governed diffusion combustion.
4. Methane was found to moderately increase the pilot-fuel burning time t_v. Generally, at the same mixing state of pilot-fuel at ignition, the cases with higher ϕ_{CH4} were found to have a higher value of t_v. This trend was attributed to the chemical influence of methane reducing the pilot-fuel reactivity. Furthermore, at otherwise unchanged charge conditions the influence of methane prolonging the ID reduces the pilot-fuel equivalence ratio at ignition. This leads to an overall lower reactivity of mixture at ignition, thus increasing the t_v.
5. Pilot-fuel injection strategy influences the HRR_{pilot}^{MAX}. Particularly in the dual-fuel cases a clear oxygen-availability limit on the HRR_{pilot}^{MAX} was observed: the HRR_{pilot}^{MAX} for most dual-fuel cases (except close to lean-out) was proportional to the initiated spray volume at ignition. Lack of variation from this proportionality indicates oxygen to be the limiting reactant in combustion.
6. With increasing ϕ_{CH4} a very strong increase of the HRR_{pilot}^{MAX} has been observed and attributed to the simultaneous combustion of methane entrained in the pilot-spray volume. This trend was consistent for the whole experimental matrix except in cases with reduced [O_2] representing EGR.
7. The influence of reduced [O_2] on the ignition delay and the combustion duration t_v was found to be strong. At constant ID, in dual-fuel cases, up to 2 times longer t_v has been observed at 15% [O_2], compared to the 21% [O_2] cases with similar ignition delay and lower T_{SOI}. This effect is probably due to the amplified chemical influence of methane under reduced [O_2] conditions leading to a further reduction of the mixture reactivity.
8. The combined retarding effect of methane and reduced [O_2] on t_v exhibits itself in decreasing HRR_{pilot}^{MAX} with increasing ϕ_{CH4}. A factor of 3–4 lower HRR_{pilot}^{MAX} values at 15% [O_2], compared to the cases with 21% [O_2] at comparable ignition delay, indicate that this is not the effect of oxygen-availability limitation as reported for the 21% [O_2] cases.

The findings about the transition behavior of the dual-fuel combustion, based on the HRR analysis in combination with experimentally investigated mixture state of the pilot-fuel, reveal a first insight into the involved processes. In particular, the mixture reactivity has been identified to be an essential parameter during the combustion mode transition. Table 3 summarizes the influence of charge and injection parameters on the pilot-fuel combustion behavior as characterized by the combustion metrics. To gain a further understanding of the interaction of auto-ignition and turbulent mixing (stratification, local distribution), in Part 2 of this study, an advanced set of optical diagnostics (CH_2O-PLIF, OH* chemiluminescence, and Schlieren imaging) has been applied to study the combustion transition. Furthermore, the experimental results are underlined and corroborated with numerical calculations (homogenous reactor model as well as simulations of the laminar flame speed) of various methane/dodecane/air mixtures. This enables a further discussion regarding the influence of methane on the chemical and/or physical driven sub-processes governing the dual-fuel combustion transition.

Acknowledgements

Financial support from the Competence Center for Energy and Mobility (CCEM, project “ScheDual”) and the Swiss Federal Office of Energy (Grant SI/501123-01) is gratefully acknowledged.

Table 3
Summary of the observed influences of charge and injection parameters on pilot-fuel combustion metrics: ID, tv and peak-HRR. Symbol interpretation: Arrow direction – increasing or decreasing influence. Number of arrows (1 up to 3) – effect strength.

Parameter/Influence	Ignition Delay	Pilot-fuel combustion duration t_v	HRR_{pilot}^{MAX}
ϕ_{CH4}	↗↗	↗↗ (↗↗↗ when combined with reduced $[O_2]$)	↗↗↗ Reduced influence at high T_{SOI}, or close to misfire (short ET, low T_{SOI})
T_{SOI}	↘	→	↘ Less time for entrainment of methane
EGR: Decreasing charge $[O_2]$	↗	↗↗↗ (↗ at $\phi_{CH4} = 0$) Amplified by the effect of methane	↘↘ (↘ at $\phi_{CH4} = 0$) Strongly reduced mixture reactivity
Pilot injection (ET/p_{inj})	↗ (↓ with p_{inj}↑) Shorter ET and high p_{inj} lead to shorter ID	→ (Except: very long ET leads to diffusion combustion and longer t_v)	↗↗

Appendix A:. TMPD tracer-PLIF methodology

A.1: TMPD Tracer-PLIF optical setup

TMPD was selected as the tracer substance for its advantages of excitation at 355 nm, high-fluorescent yield under high temperatures, and tracer thermo-physical properties similar to the properties of n-dodecane. To prevent tracer quenching by oxygen and achieve non-reactive conditions the RCEM charge consisted of pure nitrogen. Also, the fuel-supply system was purged with a constant flow of nitrogen to prevent oxygen from dissolving in the fuel.

Fig. 14 shows the optical setup for simultaneous high-speed tracer-PLIF, Mie-scattering, and Schlieren images as applied at the RCEM. Tracer-PLIF imaging provided quantitative information on the pilot-fuel concentration within the laser-sheet plane. This information was complemented by Mie-scattering imaging information on the liquid-phase extent of the spray for every single PLIF image and by Schlieren imaging information on the overall extent of the pilot-fuel jet. The view of the three optical diagnostic methods was along the same optical axis aligned with the cylinder axis. All devices were synchronized to the electronic start of injection (eSOI, 0.36 ms before hydraulic SOI) using a programmable timing unit (LaVision HS controller).

A.1.1: TMPD tracer-PLIF

Tracer-PLIF investigations were performed under non-reactive conditions using n-dodecane pilot-fuel doped with 1.5 g/l TMPD tracer. Tracer fluorescence was excited with the 355 nm 3rd harmonic output of a high-speed diode-pumped Nd:YAG laser (Edgewave IS400) at 10 kHz rate and pulse energy of 7 mJ/pulse. The laser beam was shaped into an around 1 mm thick and 50 mm high laser-sheet using a combination of cylindrical and spherical lenses. The central 30 mm of the sheet were directed into the combustion chamber at an angle of 3.5° from the firedeck. This optimal angle was determined based on the tomographic detection of ignition delay and accounts for the pilot-fuel plume compression and shifting by the piston motion.

Fluorescence was detected using an intensified high-speed camera system (LaVision HS-IRO coupled to Photron FastCam SA1.1 camera) equipped with a 100 mm f/2.8 UV lens (Sodern Cerco). The projected pixel size was 0.11 mm/pixel. A bandpass filter (400 nm central wavelength, 50 nm full-width half-maximum) has been used to separate the PLIF signal from the scattered laser light and environment light. Intensifier gate of 100 ns was used throughout this study while the gain was adapted between 3 and 20 counts/photoelectron to prevent the camera overexposure and ensure sufficient signal-to-noise ratio. The tracer-PLIF signal was then quantified to yield fuel-concentration by accounting for the image white-field, pulse intensity, information on the total injected fuel and tracer quantum-yield dependence on temperature. The exact quantification procedure is described in detail in Section A.2.

A.1.2: Mie-scattering

Liquid-phase Mie-scattering of the 355 nm laser sheet was detected at 10 kHz using a high-speed camera (Photron FastCam SA1.1) equipped with a 105 mm f/4.1 UV lens (Coastal Optics) and 355 nm bandpass filter (10 nm FWHM, BK Interferenzoptik). Due to the abundance of scattered light

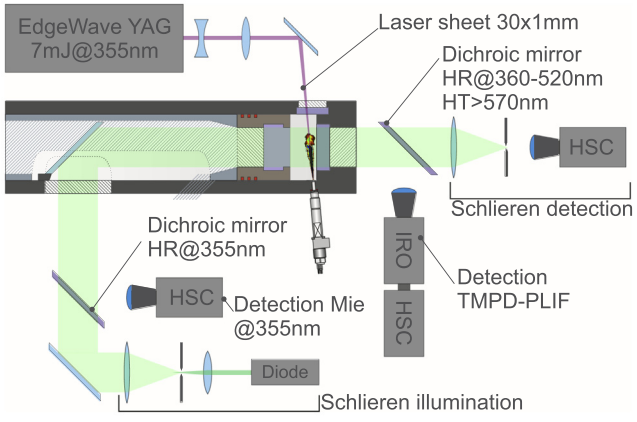

Fig. 14. Schematic of the RCEM optical arrangement for simultaneous TMPD tracer-PLIF, Mie-scattering, and Schlieren imaging.

aperture setting of f/11 was used throughout the study. The image resolution was 0.17 mm/pixel.

Images are then processed to determine the regions with presence of the liquid: First, background images acquired prior to the SOI were subtracted to remove the light scattered on the cylinder wall. Then, a threshold of 3% of the camera dynamic range was chosen to distinguish the liquid spray from the remaining background intensity in accordance to Siebers [49]. This threshold was found to reliably discriminate the liquid spray from the background scattering and camera noise.

A.1.3: Schlieren imaging

Schlieren imaging has been performed at a frame rate of 80 kHz with a projected pixel size of 0.16 mm/pixel. A fiber-coupled pulsed laser diode array (Cavilux Smart, wavelength 690 ± 10 nm, 10 ns pulse duration, 440 W output) illuminating a close-coupled diffusor plate and a 1 mm diameter pinhole has been used to generate a point light source. This light has been collimated using a 400 mm focal length achromatic lens and directed along the cylinder axis through the combustion chamber. The collimated beam has been refocused using another achromatic lens of the same type. An aperture diameter of 3 mm in the lens focal point has been used as a Schlieren stop. After passing the Schlieren stop the light was recorded with a high-speed camera (Photron Fastcam SA-X2) equipped with a Nikkor 50 mm f/1.4 lens to achieve the desired image scale. The camera exposure time was 1 μs; the lens was equipped with a 690 nm bandpass filter to suppress the flame luminosity. The aperture sizes of 1 mm and 3 mm were selected to achieve a sufficient contrast of the Schlieren images by an empirical approach, as described in [50], resulting in similar beam-divergence tolerance of the system as in other comparable studies [40,51]. Due to hardware obstructions between the piston and mirror the region closer than 22 mm to the injector orifice is not visibly accessible.

Image processing of Schlieren images was based on the adaptive background subtraction approach proposed by the Engine Combustion Network community [52]. The threshold setting in the adaptive background processing routines was chosen in an empirical procedure until the methodology reliably discriminated spray from the background.

A.2: Tracer-PLIF quantification

To obtain quantitative information on the pilot-fuel concentration using tracer-PLIF technique (1) the influence of the compression heating and evaporative cooling on the tracer quantum yield has to be accounted for, (2) the camera white-field and laser-sheet profile corrections have to be performed and (3) camera pixel-counts have to be correlated to the absolute pilot-fuel concentration. This appendix section describes the quantification approach of this study and demonstrates the quality of quantification.

First, the camera while field and laser pulse energy were addressed: A homogeneously seeded TMPD vapor has been introduced into the RCEM combustion chamber using a heated bubbler. The temperature of TMPD in the bubbler was adjusted so that similar PLIF signal intensity has been detected as during the actual fuel-vapor PLIF acquisitions. Flow through the bubbler was kept constant using a mass-flow controller. These images provided the camera white-field and laser-sheet profile correction. Additionally, such images can be used to estimate the pulse-to-pulse fluctuation of the laser-sheet. The top-hat beam of the employed laser (Edgewave IS400) with dimensions of 3 × 8 mm is very homogeneous along the short dimension and structured along the longer edge. This structure contains many peaks and varies between pulses. Therefore, the laser beam was expanded along the short dimension and focused along the long direction using a combination of cylindrical and spherical lenses. Very small shot-to-shot fluctuations of the laser sheet profile were detected and therefore we did not acquire the sheet-profile for each pulse separately. It has to be noted that along the thickness of the laser sheet rather large fluctuations are expected, however at the present resolution we do not believe that such fluctuations would influence the acquisition. Rather small pulse-energy fluctuations (3% rms) were monitored online during acquisitions with a fast photodiode and SRS Boxcar integrator.

The correction for the compression heating was done using the bulk temperature of charge taken from the thermodynamic model. The adiabatic mixing model was applied to correct the temperature of air/fuel mixture due to the evaporative cooling and mixing of the cold liquid fuel. Literature data on the fluorescence yield dependency on temperature from [53] was used after a literature review of the available datasets for TMPD: [53–55]. All datasets are in a good agreement. Nevertheless, only [53] measured the fluorescence yield over the whole temperature range of interest in this study using a setup with a short residence time of tracer to avoid the tracer thermal decomposition. The temperature and the fuel concentration were then determined iteratively using the adiabatic mixing according to the procedure proposed by Bruneaux et al. [56].

In the last stage, the camera pixel-counts were related to the absolute fuel concentration. Literature applying tracer-PLIF for sprays in constant volume chamber [56,57] suggests using the total injected fuel mass after the end of injection and axi-symmetric assumption to iteratively calibrate the detected tracer signal into fuel-concentration which integrated equals the injected fuel mass. In the case of RCEM with the piston movement during the injection, the axi-symmetric assumption might not apply anymore. Also, part of the fuel-spray will be shifted outside of the laser sheet. Therefore measurements were performed at 7 laser-sheet positions at 2 mm spacing parallel to the cylinder head surface, as drawn in Fig. 15. This way the whole spray extent was captured by these planes. Calibration was then performed by summing the fuel-concentration from all 7 planes together and the pixel-count to fuel concentration adapted so that the total fuel-concentration was captured correctly.

Considering several laser-sheet planes and different camera-gain and aperture settings necessary for different acquisitions, a reference PLIF signal was needed for different camera settings. Again the PLIF signal of the homogeneously seeded TMPD vapor was used for this purpose and was acquired after each change of the camera settings or laser-sheet shift. The temperature of the bubbler was kept constant to achieve constant tracer concentration.

As a measure of the quality of PLIF quantification, the temporal evolution of the total detected fuel-vapor is plotted in Fig. 16 and compared to the total injected mass from the injection-rate analyzer. The time at 1.5 ms aSOI was selected as the reference point at which the tracer-PLIF was calibrated. In case of perfect quantification after EOI (end of injection) the total fuel concentration should remain constant. In the interval between the end of injection and 2.5 ms aSOI, the quantification was deemed successful. However, shortly before EOI, up to 20% overshoot of the total mass was detected. This initial overshoot was attributed to scattering of very intense liquid-spray PLIF signal on the combustion chamber walls. We were unable to remove this interference efficiently. Beyond 2.5 ms aSOI the pilot-spray becomes very dilute, charge temperature very high (exceeding 1000 K) and the signal very weak. The large contribution of noise is believed to contribute to this overprediction late in the cycle.

Appendix B:. Heat Release Rate analysis

The cylinder-charge bulk temperature evolution as well as the combustion heat release rate (HRR) have been estimated using an in-house

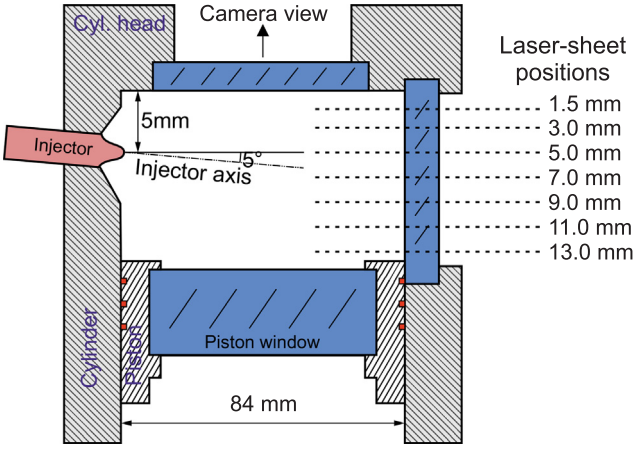

Fig. 15. Sketch of the laser-sheet positions for quantification of tracer-PLIF images based on the total injected mass. Please note that the sketch proportions do not correspond to the actual geometry.

thermodynamic model accounting for compression, wall heat losses, crevice volumes and piston rings blow-by. In the following, the processing steps and model settings are introduced.

First, the pressure trace from the piezo-electric sensor was pegged using the piezo-resistive sensor information. A offset has been added to the piezo-electric sensor read-out so that values from both pressure sensors agreed just before rapid compression was initiated. In the second step, the cylinder pressure trace has been filtered using a Savitzky-Golay filter with 3rd order polynomial fitting. In the time interval −0.2 to 0.3 ms from ID a filter frame length of 20 points (0.2 ms) has been selected so that the rapid HRR rise around ignition was not filtered out. Outside of this interval, a longer filter frame of 100 points (1 ms) was used in order to suppress the acoustic ringing in the cylinder. The filtered pressure trace and cylinder position trace were then given as an input to the HRR model.

Crevice model assuming the trapped gases temperature to adapt to cylinder wall temperature was used; the piston-ring blow-by estimated by a labyrinth sealing model from [58]. The volume of crevices and piston-ring blow-by coefficients were estimated based on the design tolerances of the RCEM. Wall heat losses were estimated using a modified Woschni equation. Adaptations to the relation were needed considering the quiescent RCEM flow field and different piston speed evolution than in engines. Eq. (1) describes the heat transfer coefficient α_w model for the RCEM:

$$\alpha_w = D^{-0.2}\cdot\left(\frac{P}{9.81 * 10^4}\right)^{0.8}\cdot T^{-0.53}\cdot\left(\left(C_0 + C_{Vol}\cdot\frac{dV}{dt}\cdot\frac{4}{\pi\cdot D^2}\cdot\left(\frac{1}{\frac{V}{V_H}}\right)^{C_H}\right) + C_2\cdot\frac{V_H\cdot T_1}{V_1\cdot P_1}\cdot(P - P_s)\right)^{0.8} \quad (1)$$

Here, V describes the instantaneous RCEM cylinder volume, V_H the displacement volume, P the cylinder pressure (in Pa) and T is the bulk RCEM gas temperature. D is the RCEM bore, and V_1, P_1, *and* T_1 describe the conditions in BDC prior to compression. The term $(P - P_S)$ is the difference in cylinder pressure between a compression stroke and actual reactive stroke and describes the increase of the wall heat losses due to combustion. This model includes the tuning constants C_0, C_{Vol} and C_2 related to different contributions to the wall heat losses. Constant C_0 relates to the heat transfer from the quiescent hot bulk gas over the boundary layer to the cylinder walls. The term related to the C_{Vol} accounts for the additional heat losses due to turbulence generated by the piston motion (wall shedding vortex) and the term related to C_2 describes the increase of heat losses due to combustion.

In order to reliably predict the HRR, the wall-heat loss model had to be tuned. Tuning constants C_0 and C_{Vol} were adjusted based on the non-reactive compression stroke acquisitions so that the modeled HRR prediction without combustion was as close to zero as possible. In the next phase, the constant C_2 was tuned so that the HRR model accurately predicted the cumulative HRR in air (equal to the LHV of the pilot injection). Since no information was available on the heat losses in the dual-fuel cases the same value of C_2 has been used also in methane/air mixture.

The single-zone thermodynamic model for HRR calculation was used assuming stoichiometric conditions of the zone. Specific enthalpies were calculated using the ideal gas assumption. After the heat-loss model constants were determined, all experimental investigations were processed with

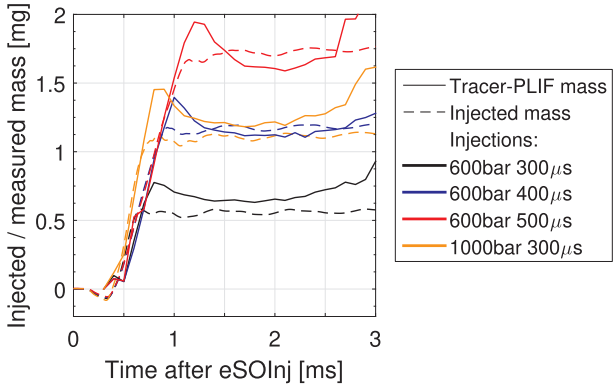

Fig. 16. Tracer-PLIF calibration: the temporal evolution of the total detected fuel-mass compared to the injected fuel mass.

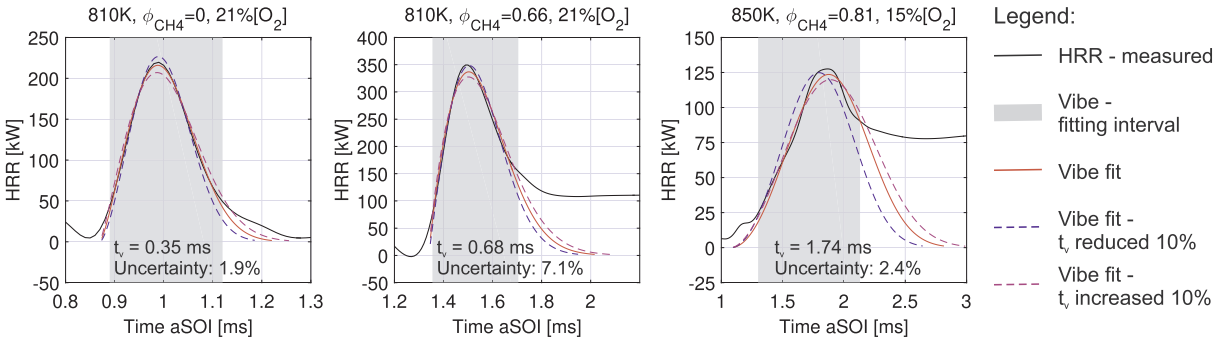

Fig. 17. Demonstration of Vibe-fit uncertainty: measured HRR in black compared to the Vibe-fit (red) and Vibe-fit with restrained values of t_v increased (violet) or decreased (blue) by 10%. The time interval used for Vibe fit is shadowed gray. Cases with ET = 400 μs: left: diesel case, T_{SOI} = 810 K, middle: ϕ_{CH4} = 0.66, T_{SOI} = 810 K, right: EGR case, 15% [O_2], ϕ_{CH4} = 0.81, T_{SOI} = 850 K. (For interpretation of the references to color in this figure legend, the reader is referred to the web version of this article.)

the same model settings using automated routines.

Appendix C:. Vibe-fit uncertainties

This appendix section addresses the uncertainties related to the determination of HRR metrics based on the Vibe-fitting function. As described in Section 2.3 and definition of combustion metrics, the largest uncertainty is related to the shape parameter m_v. This propagates also into the uncertainty of Vibe-fit combustion duration. The 95% confidence bonds of the metric t_v spread from 1.6% up to 8.5%, depending on how well the Vibe-function matches the experimentally observed HRR. The uncertainty band of the pilot-combustion cumulative HRR is somewhat larger since it depends both on m_v and t_v – it spreads from 3.4% to 11.7%.

The uncertainty of the combustion metrics is dependent on how accurate the Vibe function reproduces the experimental HRR and at which level the HRR stabilizes after the pilot-fuel is consumed – the larger the HRR after the pilot-fuel burning, the more the pilot-fuel HRR is masked by the premixed flame propagation and the prolonged interval of the pilot-fuel HRR is interpolated instead of fitted based on the experimental HRR. This is demonstrated on Fig. 17 for three select cases: diesel case with no HRR after the pilot-fuel is burnt, dual-fuel case with ϕ_{CH4} = 0.66 and an EGR case (15% [O_2], ϕ_{CH4} = 0.81) with high premixed-fuel HRR relative to the peak HRR. The experimental HRR is compared to three Vibe fits – an original fit, and two fit results where the t_v was restrained to 90% and 110% of the initial value while the fitting routine determined other Vibe function parameters. In the cases when the uncertainty of the combustion metrics is low, such restriction of the metric will lead to an obviously misaligned curve. On the other hand, in cases with high uncertainty of the combustion metrics the different combinations of Vibe parameters still lead to a reasonable fit to the experimental curve.

In the diesel case (Fig. 17 left) the fitting interval covers the whole interval with high HRR and the Vibe-fit is well aligned with the experimental trace. The uncertainty of t_v is low at 1.9%. When the fit is restrained to a different value of t_v the resulting traces are visibly misaligned. Contrary, in the dual-fuel case the fitting interval is shorter than the fitted value of t_v, and the premixed fuel to a certain extent masks the HRR from the pilot-fuel combustion. This leads to a higher uncertainty of t_v (7.1%), and if the value of t_v is restrained to a perturbated value, the resulting Vibe-fits still reasonably reproduce the experiment. This leads to wider confidence bonds of the fitted values. Also, when looking at an EGR case with relatively high HRR from the premixed fuel combustion, much shorter fitting interval compared to the value of t_v is visible. However, the slow and steady HRR rise rate seems to be characteristic enough that the uncertainty of the fitted metrics remains low at 2.4%. This is visible also from the fit results with restrained values of t_v, which show worse agreement with the experiment than the unrestrained fit.

References

[1] Wei Lijiang, Geng Peng. A review on natural gas/diesel dual fuel combustion, emissions and performance. Fuel Process Technol 2016;142:264–78. https://doi.org/10.1016/j.fuproc.2015.09.018.

[2] Yang B, Xi C, Wei X, Zeng K, et al. Parametric investigation of natural gas port injection and diesel pilot injection on the combustion and emissions of a turbo-charged common rail dual-fuel engine at low load. Appl Energy 2015;143(Supplement C):130–7. https://doi.org/10.1016/j.apenergy.2015.01.037.

[3] Liu J, Yang F, Wang H, Ouyang M, et al. Effects of pilot fuel quantity on the emissions characteristics of a CNG/diesel dual fuel engine with optimized pilot injection timing. Appl Energy 2013;110(Supplement C):201–6. https://doi.org/10.1016/j.apenergy.2013.03.024.

[4] Zhou L, Liu Y-F, Wu C-B, Sun L, et al. Effect of the diesel injection timing and the pilot quantity on the combustion characteristics and the fine-particle emissions in a micro-diesel pilot-ignited natural-gas engine. Proc Inst Mech Eng, Part D: J Automobile Eng 2013;227(8):1142–52. https://doi.org/10.1177/0954407013480452.

[5] Magno A, Mancaruso E, Vaglieco BM. Combustion analysis of dual fuel operation in single cylinder research engine fuelled with methane and diesel. SAE Technical Paper 2015-24-2461 2015. https://doi.org/10.4271/2015-24-2461.

[6] Abdelaal MM, Hegab AH. Combustion and emission characteristics of a natural gas-fueled diesel engine with EGR. Energy Convers Manage 2012;64:301–12. https://doi.org/10.1016/j.enconman.2012.05.021.

[7] Sun L, Liu Y, Zeng K, Yang R, et al. Combustion performance and stability of a dual-fuel diesel–natural-gas engine. Proc Inst Mech Eng, Part D: J Automobile Eng 2014;229(2):235–46. https://doi.org/10.1177/0954407014537814.

[8] Papagiannakis RG, Hountalas DT. Experimental investigation concerning the effect of natural gas percentage on performance and emissions of a DI dual fuel diesel engine. Appl Therm Eng 2003;23(3):353–65. https://doi.org/10.1016/S1359-4311(02)00187-4.

[9] Papagiannakis RG, Hountalas DT. Combustion and exhaust emission characteristics of a dual fuel compression ignition engine operated with pilot Diesel fuel and natural gas. Energy Convers Manage 2004;45(18):2971–87. https://doi.org/10.1016/j.enconman.2004.01.013.

[10] Lounici Mohand Said, Loubar Khaled, Tarabet Lyes, Balistrou Mourad, Niculescu Dan-Catalin, Tazerout Mohand. Towards improvement of natural gas-diesel dual fuel mode: an experimental investigation on performance and exhaust emissions. Energy 2014;64:200–11. https://doi.org/10.1016/j.energy.2013.10.091.

[11] Abd Alla GH, Soliman HA, Badr OA, Abd Rabbo MF. Effect of pilot fuel quantity on the performance of a dual fuel engine. Energy Convers Manage 2000;41(6):559–72. https://doi.org/10.1016/S0196-8904(99)00124-7.

[12] Abd Alla GH, Soliman HA, Badr OA, Abd Rabbo MF. Effect of injection timing on the performance of a dual fuel engine. Energy Convers Manage 2002;43(2):269–77. https://doi.org/10.1016/S0196-8904(00)00168-0.

[13] Nithyanandan K, Gao Y, Wu H, Lee C-F, et al. An optical investigation of multiple diesel injections in CNG/diesel dual-fuel combustion in a light duty optical diesel engine. SAE Technical Paper 2017-01-0755 2017. https://doi.org/10.4271/2017-01-0755.

[14] Pettinen R, Kaario O, Larmi M. Dual-fuel combustion characterization on lean conditions and high loads. SAE Technical Paper 2017-01-0759 2017. https://doi.

org/10.4271/2017-01-0759.
[15] Dronniou N, Kashdan J, Lecointe B, Sauve K, et al. Optical investigation of dual-fuel CNG/Diesel combustion strategies to reduce CO_2 emissions. SAE Int J Engines 2014;7:873–87. https://doi.org/10.4271/2014-01-1313.
[16] Zhang Y, Ghandhi J, Rothamer D. Effects of fuel chemistry and spray properties on particulate size distributions from dual-fuel combustion strategies. SAE Int J Engines 2017;10(4):1847–58. https://doi.org/10.4271/2017-01-1005.
[17] Ahmad Z, Aryal J, Ranta O, Kaario O, et al. An optical characterization of dual-fuel combustion in a heavy-duty diesel engine. SAE Technical Paper 2018-01-0252 2018. https://doi.org/10.4271/2018-01-0252.
[18] Egúsquiza JC, Braga SL, Braga CVM. Performance and gaseous emissions characteristics of a natural gas/diesel dual fuel turbocharged and aftercooled engine. J Braz Soc Mech Sci Eng 2009;31:142–50. https://doi.org/10.1590/S1678-58782009000200007.
[19] Schlatter S, Schneider B, Wright Y, Boulouchos K. Experimental study of ignition and combustion characteristics of a diesel pilot spray in a lean premixed methane/air charge using a rapid compression expansion machine. SAE Technical Paper 2012–01-0825 2012. https://doi.org/10.4271/2012-01-0825.
[20] Salaun E, Apeloig J, Grisch F, Yvonnet C-E, et al. Optical investigation of ignition timing and equivalence ratio in dual-fuel CNG/diesel combustion. SAE Technical Paper 2016-01-0772 2016. https://doi.org/10.4271/2016-01-0772.
[21] Srna A, Bruneaux G, von Rotz B, Bombach R, et al. Optical investigation of sooting propensity of n-dodecane pilot/lean-premixed methane dual-fuel combustion in a rapid compression-expansion machine. SAE Technical Paper 2018–01-0258 2018. https://doi.org/10.4271/2018-01-0258.
[22] Srna A, Barro C, Herrmann K, Möri F, et al. POMDME as an alternative pilot fuel for dual-fuel engines: optical study in a RCEM and application in an automotive size dual-fuel diesel engine. SAE Technical Paper 2018–01-1734 2018. https://doi.org/10.4271/2018-01-1734.
[23] Rochussen J, Yeo J, Kirchen P. Effect of fueling control parameters on combustion and emissions characteristics of diesel-ignited methane dual-fuel combustion. SAE Technical Paper 2016-01-0792 2016. https://doi.org/10.4271/2016-01-0792.
[24] Karim Ghazi A. Combustion in gas-fueled compression ignition engines of the dual fuel type. Int Combust Engines 2010:213–35. https://doi.org/10.1002/9783527628148.hoc047.
[25] Srna A, Bolla M, Wright YM, Herrmann K, et al. Effect of methane on pilot-fuel autoignition in dual-fuel engines. Proc Combust Inst 2018;37. https://doi.org/10.1016/j.proci.2018.06.177.
[26] Barro C, Nani C, Hutter R, Boulouchos K. Spray model based phenomenological combustion description and experimental validation for a dual fuel engine. SAE Technical Paper 2017-24-0098 2017. https://doi.org/10.4271/2017-24-0098.
[27] Kahila H, Wehrfritz A, Kaario O, Vuorinen V. Large-eddy simulation of dual-fuel ignition: diesel spray injection into a lean methane-air mixture. Combust Flame 2019;199:131–51. https://doi.org/10.1016/j.combustflame.2018.10.014.
[28] Liu Z, Karim GA. The ignition delay period in dual fuel engines. SAE Technical Paper 950466 1995. https://doi.org/10.4271/950466.
[29] Rochussen Jeremy, Kirchen Patrick. Characterization of reaction zone growth in an optically accessible heavy-duty diesel/methane dual-fuel engine. Int J Engine Res 2019;20(5):483–500. https://doi.org/10.1177/1468087418756538.
[30] Soriano BS, Richardson ES, Schlatter S, Wright YM. Conditional moment closure modelling for dual-fuel combustion engines with pilot-assisted compression ignition. SAE Technical Paper 2017–01-2188 2017. https://doi.org/10.4271/2017-01-2188.
[31] Soriano BS, Richardson ES. Investigation of flame propagation in autoignitive blends of n-heptane and methane fuel. Combust Theor Model 2019. https://doi.org/10.1080/13647830.2019.1614228.
[32] Khosravi M, Rochussen J, Yeo J, Kirchen P, et al. Effect of fuelling control parameters on combustion characteristics of diesel-ignited natural gas dual-fuel combustion in an optical engine. ASME 2016 Int Combust Engine Div Fall Tech Conf 2016.
[33] Barro C, Lucjan A, Li Z, Kyrtatos P, et al. Development and experimental validation of a fast spray ignition model for diesel engines using insights from CFD spray calculations. SAE Int J Fuels Lubr 2017;10(2):304–17. https://doi.org/10.4271/2017-01-0812.
[34] Kokjohn SL, Musculus MPB, Reitz RD. Evaluating temperature and fuel stratification for heat-release rate control in a reactivity-controlled compression-ignition engine using optical diagnostics and chemical kinetics modeling. Combust Flame 2015;162(6):2729–42. https://doi.org/10.1016/j.combustflame.2015.04.009.
[35] Liu H, Tang Q, Ran X, Fang X, et al. Optical diagnostics on the reactivity controlled compression ignition (RCCI) with micro direct-injection strategy. Proc Combust Inst 2018. https://doi.org/10.1016/j.proci.2018.06.180.
[36] Reitz RD, Duraisamy G. Review of high efficiency and clean reactivity controlled compression ignition (RCCI) combustion in internal combustion engines. Prog Energy Combust Sci 2015;46:12–71. https://doi.org/10.1016/j.pecs.2014.05.003.
[37] Vallinayagam R, An Y, Vedharaj S, Sim J, et al. Naphtha vs. dieseline – The effect of fuel properties on combustion homogeneity in transition from CI combustion towards HCCI. Fuel 2018;224:451–60. https://doi.org/10.1016/j.fuel.2018.03.123.
[38] Goyal H, Kook S, Ikeda Y. The influence of fuel ignition quality and first injection proportion on gasoline compression ignition (GCI) combustion in a small-bore engine. Fuel 2019;235:1207–15. https://doi.org/10.1016/j.fuel.2018.08.090.
[39] Kammermann T, Koch J, Wright YM, Soltic P, et al. Generation of turbulence in a RCEM towards engine relevant conditions for premixed combustion based on CFD and PIV investigations. SAE Int J Engines 2017;10(4). https://doi.org/10.4271/2017-24-0043.
[40] Schlatter S, Schneider B, Wright YM, Boulouchos K. N-heptane micro pilot assisted methane combustion in a Rapid Compression Expansion Machine. Fuel 2016;179:339–52. https://doi.org/10.1016/j.fuel.2016.03.006.
[41] Musculus MP, Kattke K. Entrainment waves in diesel jets. SAE Int J Engines 2009;2:1170–93. https://doi.org/10.4271/2009-01-1355.
[42] Desantes JM, Pastor JV, Garcia-Oliver JM, Pastor JM. A 1D model for the description of mixing-controlled reacting diesel sprays. Combust Flame 2009;156(1):234–49. https://doi.org/10.1016/j.combustflame.2008.10.008.
[43] Kook S, Pickett LM. Liquid length and vapor penetration of conventional, Fischer-Tropsch, coal-derived, and surrogate fuel sprays at high-temperature and high-pressure ambient conditions. Fuel 2012;93:539–48. https://doi.org/10.1016/j.fuel.2011.10.004.
[44] Pickett Lyle M, Manin Julien, Genzale Caroline L, Siebers Dennis L, Musculus Mark PB, Idicheria Cherian A. Relationship between diesel fuel spray vapor penetration/dispersion and local fuel mixture fraction. SAE Int J Engines 2011;4(1):764–99. https://doi.org/10.4271/2011-01-0686.
[45] Malbec L-M, Eagle WE, Musculus MPB, Schihl P. Influence of injection duration and ambient temperature on the ignition delay in a 2.34L optical diesel engine. SAE Int J Engines 2015;9(1):47–70. https://doi.org/10.4271/2015-01-1830.
[46] Miles PC, Sahoo D, Busch S, Trost J, et al. Pilot injection ignition properties under low-temperature, dilute in-cylinder conditions. SAE Int J Engines 2013;6(4):1888–907. https://doi.org/10.4271/2013-01-2531.
[47] Idicheria CA, Pickett LM. Ignition, soot formation, and end-of-combustion transients in diesel combustion under high-EGR conditions. Int J Engine Res 2011;12(4):376–92. https://doi.org/10.1177/1468087411399505.
[48] Idicheria CA, Pickett LM. Effect of EGR on diesel premixed-burn equivalence ratio. Proc Combust Inst 2007;31(2):2931–8. https://doi.org/10.1016/j.proci.2006.08.022.
[49] Siebers DL. Liquid-phase fuel penetration in diesel sprays. SAE Technical Paper 98-0809 1998. https://doi.org/10.4271/980809.
[50] Skeen SA, Manin J, Pickett LM. Simultaneous formaldehyde PLIF and high-speed schlieren imaging for ignition visualization in high-pressure spray flames. Proc Combust Inst 2015;35:3167–74. https://doi.org/10.1016/j.proci.2014.06.040.
[51] Bardi M, Payri R, Malbec LMC, Bruneaux G, et al. Engine combustion network: comparison of spray development, vaporization, and combustion in different combustion vessels. Atomization Sprays 2012;22(10):807–42. https://doi.org/10.1615/AtomizSpr. 2013005837.
[52] Pickett, L.M., “Engine Combustion Network.” http://www.sandia.gov/ecn/dieselSprayCombustion.php, 2013.
[53] Kim T, Beckman MS, Farrell PV, Ghandhi JB. Evaporating spray concentration measurements from small and medium bore diesel injectors. SAE Technical Paper 2002-01-0219 2002. https://doi.org/10.4271/2002-01-0219.
[54] Yeh C-N, Kamimoto T, Kosaka H, Kobori S. Quantitative measurement of 2-D fuel vapor concentration in a transient spray via laser-induced fluorescence technique. SAE Technical Paper 94-1953 1994. https://doi.org/10.4271/941953.
[55] Senda J, Kanda T, Kobayashi M, Fujimoto H. Quantitative analysis of fuel vapor concentration in diesel spray by exciplex fluorescence method. SAE Technical Papers 970796 1997. https://doi.org/10.4271/970796.
[56] Bruneaux G. Mixing process in high pressure diesel jets by normalized laser induced exciplex fluorescence part I: free jet. SAE Technical Paper 2005-01-2100 2005. https://doi.org/10.4271/2005-01-2100.
[57] Desantes JM, Pastor JV, Pastor JM, Juliá JE. Limitations on the use of the planar laser induced exciplex fluorescence technique in diesel sprays. Fuel 2005;84:2301–15. https://doi.org/10.1016/j.fuel.2005.05.009.
[58] Seume J, Mailach R. Grundlagen der Strömungsmaschinen“, in Dubbel: Taschenbuch für den Maschinenbau. Berlin Heidelberg: Springer Berlin, Heidelberg; 2014. p. 1250–77.